International Journal of Earth Sciences (2018) 107:1097–1126
https://doi.org/10.1007/s00531-018-1595-9

ORIGINAL PAPER

Spatial coincidence and similar geochemistry of Late Triassic and Eocene–Oligocene magmatism in the Andes of northern Chile: evidence from the MMH porphyry type Cu–Mo deposit, Chuquicamata District

Marcos Zentilli[1] · **Victor Maksaev**[2] · **Ricardo Boric**[3] · **Jessica Wilson**[1,4]

Received: 19 March 2017 / Accepted: 22 February 2018 / Published online: 12 March 2018

Abstract
The MMH porphyry type copper–molybdenum deposit in northern Chile is the newest mine in the Chuquicamata District, one of largest copper concentrations on Earth. Mineralized Eocene–Oligocene porphyry intrusions are hosted by essentially barren Triassic granodiorites. Despite a century of exploitation, geologists still have problems in the mine distinguishing the Triassic granodiorite from the most important ore-carrying Eocene porphyries in the district. To resolve the problem, internally consistent high-quality geochemical analyses of the Triassic and Tertiary intrusives were carried out: explaining the confusion, they show that the rock units in question are nearly identical in composition and thus respond equally to hydrothermal alteration. In detail, the only difference in terms of chemical composition is that the main Eocene–Oligocene porphyries carry relatively less Fe and Ni. Unexpectedly, the mineralized Eocene–Oligocene porphyries have consistently less U and Th than other Tertiary intrusions in the district, a characteristic that may be valuable in exploration. The supergiant copper–molybdenum deposits in the Central Andes were formed within a narrow interval between 45 and 31 Ma, close to 7% of the 200 My duration of "Andean" magmatism, which resulted from subduction of oceanic lithosphere under South America since the Jurassic. Although recent work has shown that subduction was active on the margin since Paleozoic times, pre-Andean (pre-Jurassic) "Gondwanan" magmatism is often described as being very different, having involved crustal melting and the generation of massive peraluminous rhyolites and granites. This study shows that the indistinguishable Late Triassic and Eocene–Oligocene intrusions occupy the same narrow NS geographic belt in northern Chile. If it is accepted that magma character may determine the potential to generate economic Cu–Mo deposits, then Late Triassic volcano-plutonic centres in the same location in the South American margin could have contained valuable ore deposits, although their preservation will depend on the level attained by pre-mid Jurassic erosion. Both Late Triassic and Eocene–Oligocene magmatic events occurred during the waning stages of vigorous volcano-plutonic cycles, and both preceded apparent gaps in igneous activity (Rhaetian and post-Oligocene), abrupt lateral shifts of the volcanic front and radical changes in the character of the magmas generated. Both Late Triassic and Eocene–Oligocene intrusions were emplaced along the same narrow strip of crust; it is probable that they both exploited the same deep crustal structures. The Eocene–Oligocene magmatic front was controlled by an orogen-parallel shear system caused by oblique subduction; it is possible that Late Triassic magmatism along the same belt had a similar setting. The identified Rhaetian gap in subduction and magmatism may have widespread implications.

Keywords Porphyry type Cu–Mo · Northern Chilean Andes · Eocene–Oligocene · Late Triassic Rhaetian · Andean Subduction · Geochemistry · Chuquicamata District · MMH mine

Introduction

This paper summarizes geochemical data from the recently opened Ministro Hales Mine (*Mina Ministro Hales*; formerly *Mansa Mina;* subsequently referred to as MMH) exploiting a porphyry type Cu–Mo type deposit (henceforth PCD) in

✉ Marcos Zentilli
zentilli@dal.ca

Extended author information available on the last page of the article

the Chuquicamata District of northern Chile (Figs. 1, 2) one of the largest natural copper concentrations on Earth (e.g., Camus 2003). This study arose from a need to develop a practical method to help differentiate between relatively barren Triassic host intrusives from mineralized Eocene–Oligocene porphyries; embarrassingly, despite one century of mining, these rock units are regularly misidentified during routine mapping and core logging (e.g., Ambrus 1979; Zentilli 2012), even by experienced geologists, to the point that Proffett (2008) suggested that "the ultimate criterion for distinction between these units may be U–Pb zircon dating". The presence of intrusives of Triassic age as barren hosts to highly mineralized Eocene–Oligocene plutons in the Chuquicamata District has been recognized by extensive field mapping, textural and mineralogical studies and geochronology (e.g., Ambrus 1979; Boric et al. 1990; Ossandón

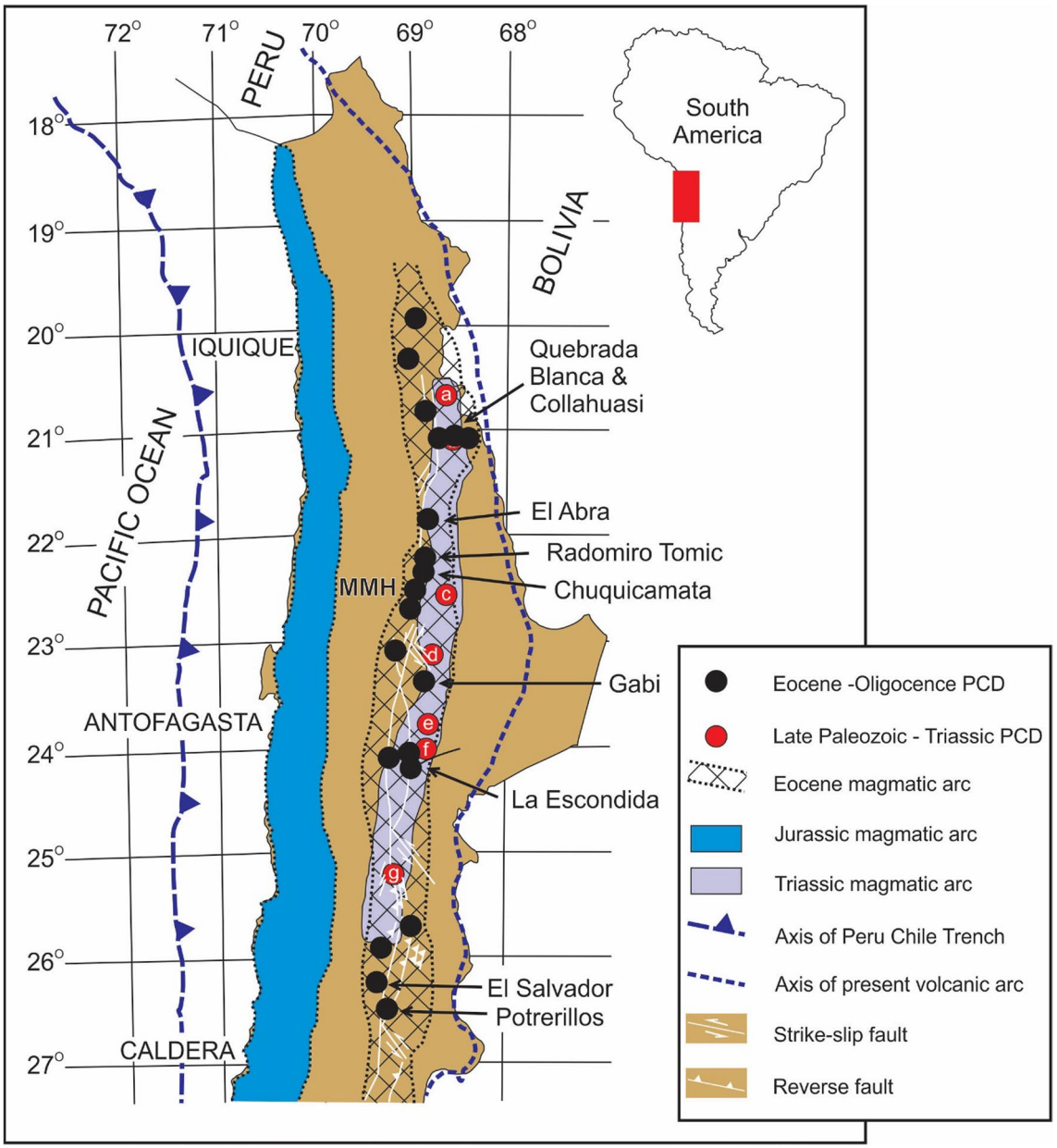

Fig. 1 Northern Chile showing the overlap of the Eocene–Oligocene and the Triassic magmatic fronts within the Domeyko Cordillera, separate from the Jurassic magmatic front along the coast. It also shows the location of giant Eocene–Oligocene porphyry type Cu–Mo deposits (PCD), and a few of the many known Permo-Triassic mineralized showings: **a** Characolla (201 Ma), **b** El Loa (284–239 Ma); **c** Lilian (290–260 Ma); **d** Tornasol (294–198 Ma); **e** Lila (213–195 Ma); **f** El Jardín (216–203 Ma); and **g** Río Frío (298–285 Ma). Data from Camus (2003) and del Rey et al. (2016). Both the Triassic and Eocene magmatic arc coincide with the Domeyko Cordillera range and is affected by the orogen-parallel Domeyko Fault System

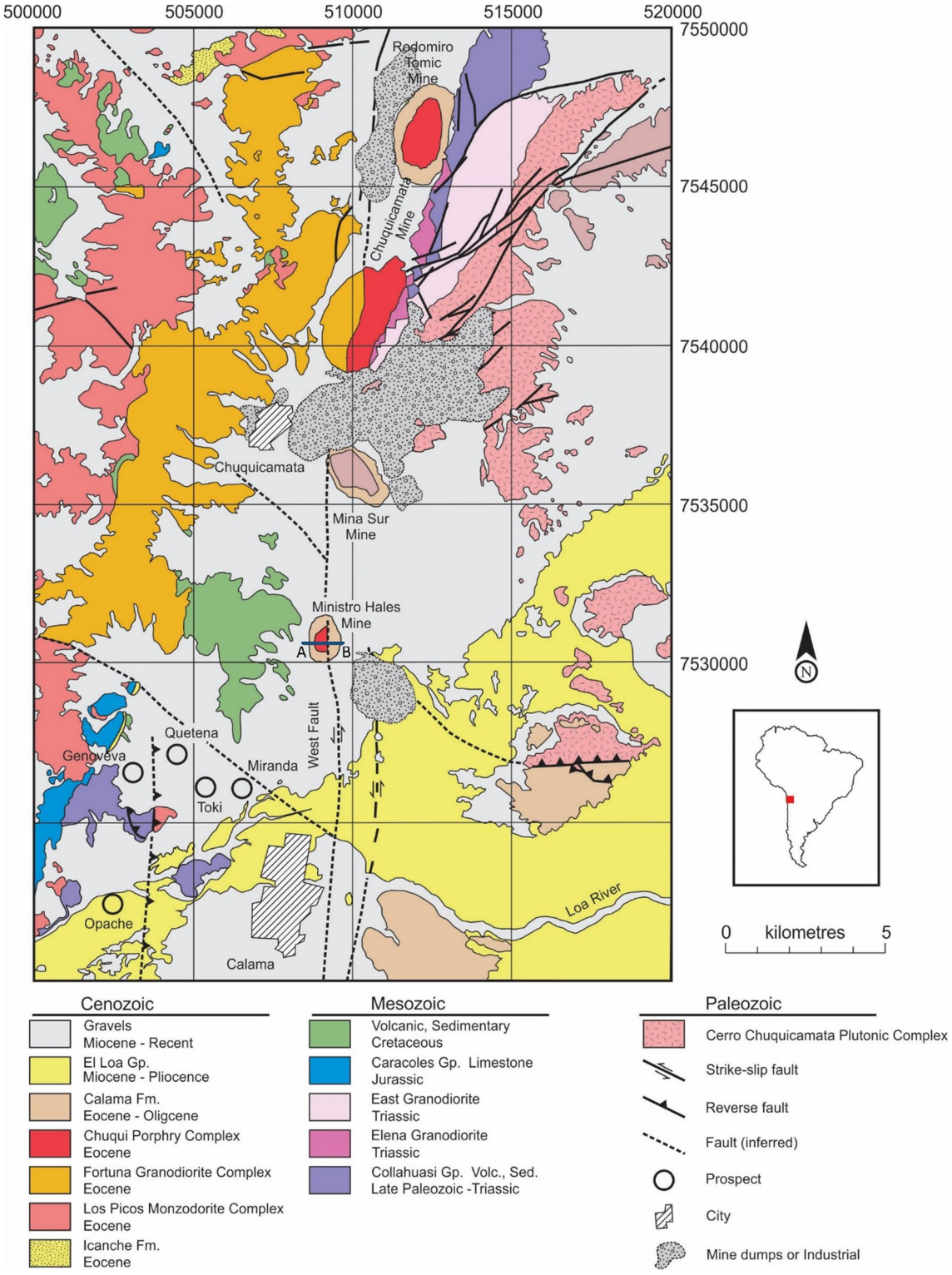

Fig. 2 Generalized geological map of the Chuquicamata District (modified from Rivera et al. 2012). Coordinates are Provisional South American 1956 UTM datum. Line A–B indicates approximate location of section in Fig. 3

et al. 2001; Wilson et al. 2011; Barra et al. 2013). However, the puzzle persists, and no high-quality analyses of the Late Triassic intrusives at Chuquicamata were available in the literature before this study.

Using a set of internally consistent analytical data for major, minor and trace elements, we find that the problem lies in that Late Triassic and Eocene–Oligocene intrusives within the MMH mine are geochemically nearly indistinguishable. Furthermore, the fact that they occupy the same narrow volcano-plutonic strip (Fig. 1) points to similar tectonic configurations and conditions of magma genesis in the pre-Andean Triassic and the Eocene–Oligocene. Both the Late Triassic and Eocene–Oligocene magmatic rocks in Chuquicamata district were formed in an Andean-type subduction environment.

The Central Andes have been used as laboratory for metallogenic studies for more than half a century (e.g., Ruiz and Ericksen 1962), owing to its anomalous concentration of the Earth's metal resources, especially Cu, and later because of the evident relation of magmatism to subduction of oceanic lithosphere under the South American continent (e.g., Farrar et al. 1970; James 1971; Sillitoe 1972, 2010; Levi 1973; Clark et al. 1976; Jordan et al. 1983; Maksaev 1990; Camus 2003; Mpodozis and Cornejo 2012). Dostal et al. (1977) were the first to discuss changes in igneous rocks through time across the northern Chilean Andes, followed by Ishihara et al. (1984), Mpodozis and Ramos (1990), Mpodozis and Kay (1992), Scheuber et al. (1994), and more recently Lucassen et al. (2006), Contreras et al. (2015), Spikings et al. (2016), del Rey et al. (2016) and Coloma et al. (2017).

The MMH deposit (Lat. 22°22′45″S; Long. 68°54′50″W; 2400 m.a.s.l.), discovered concealed under thick Cenozoic gravels (Sillitoe et al. 1996; Boric et al. 2009), is the latest mine to be developed within the Chuquicamata Cu–Mo District in the Atacama Desert (Fig. 1). Chuquicamata is one of largest copper concentrations on Earth (> 100 Mt of Cu metal resources; e.g., Barra et al. 2013) and one of the largest districts within the Eocene–Oligocene metallogenetic province along the Domeyko Cordillera of northern Chile (e.g., Ossandón and Zentilli 1997; Ossandón et al. 2001; Rivera et al. 2012). Porphyry type Cu–Mo deposits (PCD) are large, bulk-mineable, low-grade disseminated sulfide deposits formed at the roots of stratovolcanoes (e.g., Sillitoe 2010). In this region PCD are ascribed to calc-alkaline magmatism of the "Andean" cycle, generated during the last 200 Ma, from the Early Jurassic to the present. In northern Chile, there are many hundreds of copper deposits ranging in age from Jurassic to Neogene, but supergiant PCDs were formed in only 7% of that time interval, the Eocene–Oligocene (45–31 Ma; Maksaev et al. 1988; Sillitoe 1988; Lee et al. 2017).

Magmatism in the Early Paleozoic to Late Triassic along western South America is considered to have resulted from subduction processes during a "Gondwanan" cycle (e.g., Mpodozis and Ramos 1990), but this activity would have declined during the Middle Permian. to be followed by a period of rifting and extension in the Late Triassic (Rhaetian). In a geodynamic analysis of the Central Andes of Peru, Bolivia, northern Chile and Ecuador, Jaillard et al. (2000) wrote: "no clear evidence of Triassic volcanism related to subduction has been found in this region"; all magmatism of this age was interpreted as alkaline and related to rifting and the breakup of Pangea. More recently, in an isotopic study of zircon in igneous rocks south of latitude 28°S, Hervé et al. (2014) conclude that whereas the earliest Permian rocks were generated in a subduction-related magmatic arc, it changed into an extension-related environment in the Late Triassic. González-Maurel et al. (2016) in a study within the Domeyko Cordillera, suggest uninterrupted subduction-related magmatism from Late Paleozoic to Late Triassic and development of an extensional magmatic arc from early Permian to Triassic times.

Nonetheless, several sub-economic PCD associated with Middle to Late Triassic intrusives ranging in age from 245 to 223 Ma, assumed to be related to subduction have been recognized in northern Chile, (Fig. 1; e.g., Sillitoe 1977; Camus 2003; Sillitoe and Perelló 2005; Cornejo et al. 2006; Munizaga et al. 2008; Maksaev et al. 2014). In most cases, pre-Jurassic erosion of the associated volcano-plutonic centers and overprinting by later stratigraphic cover or hydrothermal processes have obscured their existence. Tomlinson and Blanco (2008) have discussed in detail the tectonic implications of Triassic intrusions and the coincidence in space with important Eocene–Oligocene Cu–Mo PCD.

It is debated whether there was an interruption of subduction or merely a slab rollback during the Late Triassic, but it is known that subduction was re-established in northern Chile during the Early Jurassic, when a magmatic arc (Fig. 1) formed along the present coast (e.g., Mpodozis and Kay 1992; Mpodozis and Cornejo 2012; Coloma et al. 2017). Since the Jurassic the magmatic front in northern Chile migrated generally eastwards (e.g., Farrar et al. 1970; Boric et al. 1990), although in detail the Early Jurassic to mid Cretaceous progression was more complex, involving eastward and westward movements of the front by tens of kilometers (e.g., Buchelt and Tellez-Cancino 2006). In the Eocene–Oligocene the magmatic front had its axis at the longitude of the present Domeyko Cordillera (Fig. 1).

The first stages of the Andean cycle correspond to thick Jurassic porphyritic volcanic rocks and associated coastal plutons with mantle-derived magmas akin to those in island arcs, calc-alkaline to tholeiitic, with flat REE patterns (e.g., Dostal et al. 1977; Kramer et al. 2005; Parada et al. 2007). The tectonic regime involved southeast-directed oblique subduction, leading to the development of the sinistral, orogen-parallel Atacama Fault System, that culminated in the Cretaceous (e.g., Åberg et al. 1984; Cembrano et al. 2005).

Magmatism changed to andesitic as the front shifted further east in the Cretaceous and Paleocene. In the Eocene, stratovolcanoes formed during a compressive period that

coincided with north-easterly directed oblique subduction. This subduction led to the development of a dextral orogen-parallel shear system, the Domeyko Fault System, a deep fracture that controlled the ascent of magmas and hydrothermal circulation (e.g., Boric et al. 1990; Lindsay et al. 1995; Reutter et al. 1996; Tomlinson and Blanco 1997), closely overprinting the pre-existing Permian and Triassic igneous front (Fig. 1). Intrusion of the porphyries in Eocene–Oligocene times coincided with rapid exhumation of the volcanic complexes and the basement (e.g., Maksaev and Zentilli 1988, 1999; McInnes et al. 1999) and the accumulation of erosional debris of the Calama Basin (May et al. 2010; Calama Fm.; Fig. 2). The last manifestation of igneous/hydrothermal activity recorded in the Chuquicamata District was in the Oligocene (Reynolds et al. 1998), and after a period of apparent quiescence, the Neogene volcanic front developed more than 20 km to the east and extended far into Argentina (e.g., Maksaev and Zentilli 1999; Coira et al. 1982).

Judging from the recent literature (e.g., Spikings et al. 2016; del Rey et al. 2016; González-Maurel et al. 2016; Coloma et al. 2017), there is renewed interest in the geology of the Gondwanan-Andean transition in the Central Andes. This study contributes to resolution of a practical problem, pointing out previously undocumented geochemical similarities between Late Triassic and Eocene–Oligocene rocks, and suggests a new exploration tool. The results point toward a similar tectonic framework for the Central Andes in the Late Triassic (Norian) and the Eocene–Oligocene. However, it is out of the scope of this paper to discuss the detailed tectonic implications of this transition, for which the reader is directed to other specialized studies (e.g., Tomlinson and Blanco 2008; Coloma et al. 2017).

Geology

The geology of the Chuquicamata District and its mines, including MMH, have been described by Ossandón et al. (2001), Rivera et al. (2012) and Barra et al. (2013), and the detailed regional stratigraphic relationships, geology and tectonics were thoroughly analyzed by Tomlinson and Blanco (2008); therefore, only pertinent points are repeated here. A dominant structural feature in the district is the north–south, strike–slip Domeyko Fault System, which has had a complex history (e.g., Lindsay et al. 1995; Reutter et al. 1996; Dilles et al. 1997; Tomlinson and Blanco 2008). Right-lateral during ore genesis in Eocene and early Oligocene, after the formation of the Chuquicamata ore deposits (35–31 Ma), the fault experienced a left-lateral displacement of ca. 35 km that truncates the Chuquicamata ore deposit proper on its west side (accordingly West Fault—Fig. 2); this fault bounds the MMH deposit on its east side (Fig. 3). East of the West Fault, the district includes the giant Chuquicamata deposit (locally referred to as "Chuqui") and Radomiro Tomic (RT) deposits, as well as the exotic (displaced supergene) copper deposit Mina Sur (South Mine; formerly *Exótica*). Located south of Chuquicamata and west of the fault are the Mina Ministro Hales mine (MMH) and mineral deposits of the Toki cluster (Toki, Genoveva, Quetena, Miranda, and Opache; Fig. 2). Zentilli et al. (2015), based on geochronology and mineralogy, have proposed that

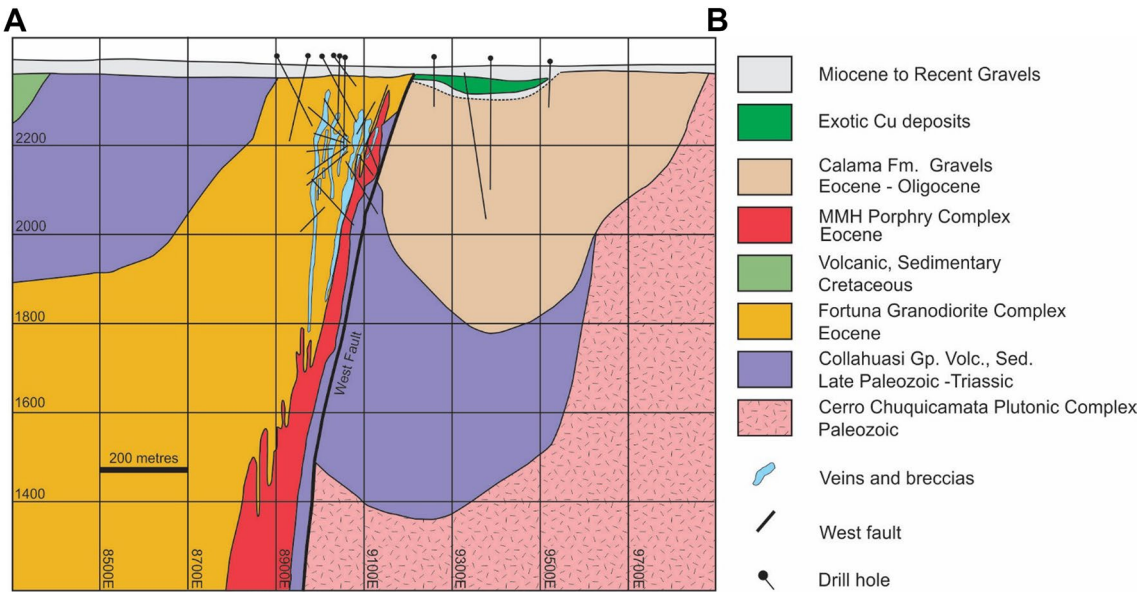

Fig. 3 Simplified geological cross-section of the MMH deposit. The MM Porphyry Complex includes bodies of Quartz Porphyry and dikes of Dacitic Porphyry (not identified in the figure). Modified from Rivera et al. (2012) and Pinget (2016)

MMH is the "missing half" of Chuquicamata, wedged in a fault loop and spared the full 35 km displacement of the West Fault regional system.

The oldest rocks in the district are Paleozoic igneous and metamorphic rocks (amphibolite and mica schists) associated with the Cerros de Chuquicamata plutonic complex (Permian granite and diorite) exposed south and east of the main Chuquicamata workings (Fig. 2), and under Cenozoic gravels east of the West Fault in the MMH mine (Fig. 3). The Collahuasi Group is composed of andesite, dacite and sandstone of Permian to Triassic age (288–231 Ma; zircon U–Pb; Tomlinson and Blanco 2008). The Triassic MM Granodiorite and equivalent Elena and Este Granodiorite in Chuquicamata are intrusive phases of the Collahuasi pre-Jurassic volcano-plutonic complexes. Unconformably overlying the eroded remnants of the above complexes lie fossiliferous marine limestone strata of Middle Jurassic age (Caracoles Group, Bajocian; Tomlinson and Blanco 2008).

West of the West Fault (Fig. 2) there are extensive outcrops of andesite and dacite lava and tuff of Early to Late Cretaceous age (Cuesta de Montecristo, Cerritos Bayos and Quebrada Mala Fms.). As described by Tomlinson and Blanco (2008), the intrusive rocks that outcrop west of the fault (Fig. 2) are the Los Picos Monzodiorite Complex (41.5–43.7 Ma, U–Pb) and the Fortuna Granodiorite Complex with granodiorite, tonalite and aplite (37–40 Ma, U–Pb). Andesitic and dacitic volcanic breccias and conglomerates of the Icanche Fm. of early-middle Eocene age outcrop northwest of the district. South of the Chuquicamata mine and east of the West Fault (Fig. 3) there are polymictic conglomerates (locally called "old gravels") containing clasts of Eocene–Oligocene igneous rocks, known as the Calama Fm. (e.g. Tomlinson and Blanco 2008). Towards the top the gravels lie mud flow deposits made of coarse sand and small angular clasts derived from Chuquicamata granodiorite and from areas located to the North; these younger gravels have been approximately dated with an ignimbrite bed (Late Miocene, 8.4 ± 0.4 Ma, K–Ar; Mortimer et al. 1978) located 5–10 m below the present surface. These gravels contain the exotic Cu deposits (Mina Sur, Fig. 2) derived from leaching of the supergene zone of Chuquicamata (e.g., Pinget 2016; Sillitoe et al. 1996). The upper beds may correlate with the Late Miocene and Pliocene limestones and siltstones of El Loa Group (Tomlinson and Blanco 2008); in the map and section (Figs. 2, 3) they are not differentiated from Quaternary alluvial and colluvial deposits.

The hypogene hydrothermal mineralization of the PCD deposits in the Chuquicamata district is Eocene to Oligocene in age (35–31 Ma; Reynolds et al. 1998; Ossandón et al. 2001; Campbell et al. 2006), and supergene processes that have altered and increased the economic value of the deposits were active until the Pliocene (e.g., Pinget 2016; Sillitoe et al. 1996). The main igneous units encountered in the Chuquicamata mine associated with potassic alteration and mineralization (Chuqui Porphyry Complex; Fig. 2) are the principal *Este Porphyry*, and other intramineral units, such as the dike-like *Oeste Porphyry* and *Banco Porphyry* (Ossandón et al. 2001; Faunes et al. 2005). At the MMH mine, located 7 km to the south, and recently interpreted as a fault-displaced fragment of Chuquicamata (Zentilli et al. 2015), the mineralized MM Porphyry Complex (Fig. 3) consists of the widespread *MM Porphyry*, relatively less voluminous units of *Quartz Porphyry* (QTZ-P) and small dikes of *Dacitic Porphyry*. The mineralization at MMH consists of disseminated porphyry type Cu and Mo sulfides, and younger Cu–Ag sulfide-rich hydrothermal breccia bodies (Fig. 3), comparable to the late enargite–chalcocite–sphalerite assemblages in Chuquicamata (e.g. Ossandón et al. 2001; Boric et al. 2009; Pinget et al. 2015). The mineral-related porphyry intrusions are hosted by Permian and Triassic intrusions and volcanic or volcano-sedimentary units. Pertinent to this paper are the Triassic *Elena and Este Granodiorites* (Fig. 2) in the Chuquicamata and RT mines and the coeval Triassic *MM Granodiorite* at MMH. The Triassic age of these intrusives has been confirmed by various geochronological methods (Tomlinson et al. 2001; Zentilli et al. 2015). Post-ore, lenticular "pebble dikes" of breccia occur within the West Fault system in the MMH deposit; clasts are angular to rounded in a clastic matrix, and barren of mineralization; they are interpreted to be products of fluidized beds during venting of highly pressurized steam; their age has not been established (Boric et al. 2009).

Methods

Representative rock samples of the main porphyries were collected from drillcore and the mine workings. Additional samples were selected from previous doctoral theses supervised by the main author (Lindsay 1997; Arnott 2003) and compared with those available from the literature (e.g., Ballard 2001; Ambrus 1979). It is practically impossible to find unaltered rocks within a PCD system, therefore veining or conspicuous alteration were removed as much as possible with a diamond saw, and any saw marks were abraded away. Analyses for major and trace elements were performed by ACTLABS of Ancaster, Ontario, Canada. Analyses were done using research-grade analytical procedures which include INAA, total digestion and ICP analysis, lithium metaborate/tetraborate fusion, and ICP. XRF was used for Ga, Pb, Sn, Nb y Rb. Sulfur was analyzed by TD-ICP and by infrared methods. One sample of MM Granodiorite (ZMMH 15) that yielded anomalous results was reanalyzed, giving identical results. In Tables 2 and 3 and figures we use the average of the two analyses.

After mineral separation, and due to time and budget constraints, only 7 out of 28 samples were considered worth dating by U–Pb TIMS; microscopy of zircon crystals reveals inherited cores, overgrowths and compositional zoning (e.g., Zentilli et al. 1994). Analyses were done by Larry Heaman at the University of Alberta, Edmonton, Canada following standard practices (e.g., Heaman et al. 2002). Some samples with complex zircons were reanalyzed using LA-ICP-MS (e.g., Simonetti et al. 2005), a method that seems more suitable for these rocks. A summary of U–Pb zircon dates (and Re–Os data on ores) is available in Zentilli et al. (2015), the detailed analytical data appear in Zentilli (2012) and are being published elsewhere (Zentilli et al. in prep).

Samples

Twenty-eight samples of representative host rocks selected from MMH core were analyzed at for major, minor, trace elements and volatiles. Representative samples from Chuquicamata and RT were analyzed using the same procedures for consistency (Table 1). Symbolizing the problem of distinguishing the Triassic from Tertiary intrusives, five of the samples that were collected in the field to represent Eocene–Oligocene porphyry according to drillhole logs, geological maps and sections and expert advice from experienced staff, yielded Triassic U–Pb zircon dates, confirming the concern of Proffett (2008) that U–Pb dating may be required to differentiate the host rocks.

Triassic rocks

The most important rock bodies that have been dated as Triassic (Ossandón et al. 2001; Tomlinson and Blanco 2008; Zentilli et al. 2015) consist of the *MM Granodiorite* at MMH mine and the *Elena and Este Granodiorites* at Chuquicamata (Figs. 2, 3).

MM Granodiorite This rock is not a porphyry, but a medium-grained hypidiomorphic-equigranular granodiorite assemblage of feldspar, quartz and chloritized biotite (Fig. 4a, b). Some phases of MM Granodiorite are quartz-rich (> 35% by volume) and others quartz-poor (< 5% by volume); mafic mineral abundance can vary from 4 to 15% by volume; some dark phases are described as Hornblende Porphyry (ZMMH-04; Table 1). MM granodiorite is universally altered, and the feldspar crystals (1.5–3 mm) are sericitized. When affected by potassic alteration, potassium feldspar megacrysts can give the rock a porphyritic appearance (Fig. 4c). The quartz is anhedral, and its abundance increases with alteration. Highly chloritized biotite occurs in irregular clusters (2–0.5 mm); remnant biotite is commonly poikiloblastic with inclusions of quartz, rutile, apatite and sulfides. However, as noted by Proffett (2008), in contrast with the younger porphyries, sphene (titanite) megacrysts are rare in the Triassic rocks. Five samples of MM Granodiorite yielded Triassic U–Pb dates (Table 1); notably, three of these five had been sampled to represent Eocene MM Porphyry. Due to the presence of inherited zircons and oscillatory zoning with varying U content, some TIMS dates have a large uncertainty; the U–Pb dates are 196.0 ± 17, 207.4 ± 7.2, 207.6 ± 2.5, 214.6 ± 6 and 229.1 ± 1.8 Ma (Carnian) by U–Pb LA-MC-ICPMS (Table 1), suggesting an age not younger than 211 Ma (Norian). Within the uncertainty the dates could have overlapped with the Rhaetian stage, previously thought to start at ~ 208.5 Ma (Cohen et al. 2017), but precise zircon U–Pb work on bracketing ash units by Wotzlaw et al. (2014), indicates that the brief Rhaetian stage extended from 205.50 ± 0.35 to 201.36 ± 0.17 Ma. We interpret the age of the *MM Granodiorite* to be Carnian to Norian; it is possible that there are undifferentiated older and younger phases as is the case in Chuquicamata.

Elena and Este Granodiorite on the east side of the Chuquicamata open pit (Fig. 2) occupy a similar geologic position as the *MM Granodiorite* at MMH (Fig. 3). They intrude metasedimentary rocks (originally sandstone, shale, minor limestone), and it is probable that there is more than one phase of each. In some parts of the open pit *Elena Granodiorite* is texturally and mineralogically indistinguishable from the Este Porphyry (e.g., Proffett 2008), and contacts are blurred, to the point that an earlier worker (Ambrus 1979) designated the unit in the contact zone "*Transition Elena-Chuqui Porphyry*". These intrusives are generally devoid of disseminated mineralization but show varying effects of alteration. Four analyses for major elements of *Elena Granodiorite* in Chuquicamata by Ambrus (1979) compared with this study indicate its chemical composition is indistinguishable from *Granodiorita MM*. The *Este Granodiorite* is equigranular, medium grained, with plagioclase, K-feldspar, quartz, biotite and hornblende and biotite. One sample of *Este Granodiorite* from the RT Mine (Z169-ME1; Table 1) was chemically analyzed here. Proffett and Dilles (2007) carried out a (SHRIMP-RG) U–Pb zircon dating study of Triassic intrusives in eastern Chuquicamata and based on weighted average dates of 231.4 ± 2.0 and 233.1 ± 2.2 Ma, concluded that both intrusive units are Late Triassic (Carnian) in age (Rivera et al. 2012).

Two unusual samples listed in Table 1 deserve notes: (A) ZMMH-04 is a dark green *Hornblende Porphyry* with rectangular chloritized hornblende phenocrysts of up to 3 mm. It is probably a different phase of the *MM Granodiorite*. (B) ZMMH-160 is an equigranular diorite sampled beyond (east of) the intersection with the West Fault. It is the most mafic rock encountered in MMH (56% SiO_2; 2.6% MgO; Tables 2, 3), and the unit contains angular xenoliths of granite from the Chuquicamata Plutonic Complex of Permian age (Fig. 2). These samples were not dated.

Table 1 Sample list and their location and assumed age

Field number	Rock unit	Notes	DHH No	From m	To m	Age Ma Zircon date U–Pb
ZMMH-15	MM GRD	Diorite	4976	1286.47	1286.60	Triassic[a]
ZMMH-05	MM GRD	Granodiorite; hornblende remnants	3173	853.75	853.86	Triassic[a]
ZMMH-50	MM GRD	Granodiorite; gray-green sericite alteration	5245	1059.55	1059.65	Triassic[a]
ZMMH-23	MM GRD	Granodiorite—"typical"; low alteration	4976	1064.00	1064.15	196.0 ± 17
ZMMH-163	MM GRD	Granodiorite—"typical"; low alteration	8561	520.90	521.10	207.6 ± 2.5
ZMMH 10	MM GRD	Granodiorite—K alteration; chlorite, calcite veinlets	5014	161.00	161.20	Triassic[a]
ZMMH-14	MM GRD	Granodiorite—mapped as MM-P; altered, mineralized alt, min	4976	1241.00	1241.12	207.4 ± 7.2
ZMMH-20	MM GRD	Granodiorite—low alteration, mineralized "ore"	4976	870.90	871.05	Triassic[a]
ZMMH-17	MM GRD	Granodiorite—quartz veinlets removed before analysis	4976	855.40	855.50	Triassic[a]
ZMMH-18	MM GRD	Granodiorite—sericite alteration, mineralized	4976	845.85	845.95	214.6 ± 6.0
ZMMH-91	MM GRD	K-alteration, A and B quartz veinlets (mapped as MM-P)	8551	1098.43	1098.74	229.1 ± 1.8
ZMMH-88	MM-P	K-alteration, A and B quartz veinlets	8551	1032.76	1033.12	Eocene[b]
ZMMH-07	MM-P	K-alteration; secondary biotite replacing hornblende	4903	1012.00	1012.25	Eocene[b]
ZMMH-21	MM-P	"Typical" MM porphyry	4976	883.20	883.24	Eocene[b]
ZMMH-96	MM-P	Mapped as feldspar porphyry within MM-P *K alt*.	8564	839.85	840.10	Eocene[b]
ZMMH-81	MM-P	K-alteration; Cu sulfides	8551	861.60	861.78	Eocene[b]
ZMMH-89	MM-P	K-alteration, A and B quartz veinlets; quartz "eyes"	8551	1069.64	1069.77	35.03 ± 0.34
ZMMH-97	QTZ-P	Highly altered dike, by major fault; quartz "eyes"	8569	617.70	617.89	35.3 ± 3.5
ZMMH-164	QTZ-P	Feldspar porphyry with fine matrix; recalls Banco P.	8806	990.30	990.50	Eocene[b]
ZMMH-11	QTZ-P	Quartz porphyry	4976	897.87	898.00	Eocene[b]
ZMMH-162	QTZ-P	Quartz porphyry; quartz "eyes"	8561	603.35	603.50	Eocene[b]
ZMMH-13	QTZ-P	"Typical" quartz porphyry	4976	1123.78	1123.90	Eocene[b]
ZMMH-12	QTZ-P	Quartz porphyry; brecciated; similar to Dac-P; Moly.	4976	1128.00	1128.12	Eocene[b]
ZMMH-76	DAC-P	Feldspar porphyry; large K-spar; argillic alteration overrgílica sobre K	8551	699.58	699.75	33.7 ± 0.8
ZMMH-09	DAC-P	Dacite dike; similar to QTZ-P	4884	158.90	159.00	Oligocene[b]
ZMMH-66	DAC-P	Dacite porphyry; quart veinlets	8551	214.95	215.08	Oligocene[b]
ZMMH-67	DAC-P	Dacite porphyry; alunite, enargite present	8551	132.12	132.30	Oligocene[b]
ZMMH-04	HRNB-P	Hornblende porphyry—probably Hb-rich MM-GRD	3173	888.50	888.63	Triassic (?)
ZMMH-160	DIORITE	Diorite with Pz granite inclusions—east of West Fault	8561	857.70	857.83	Pz or Tr (?)
Z169-ME1	GRD ESTE-RT	East Granodiorite—Radomiro Tomic Mine	9394	264.60	265.00	232.35 ± 3[c]
Z170-ME2	E-P RT	East Porphyry—Radomiro Tomic Mine	9394	329.56	329.85	ca. 35[d]
Cu-2022	E-P CHU	Este P.—Chuquicamata pit [UTM N 7537.708/E 512,130–3053 m.a.s.l. (MZ 2006)]				ca. 35[d]
Cu-1333	P-B CHU	Banco P.—Chuquicamata pit; Bench G3 (2722 m.a.s.l.) N5300/E3950 Sample D. Lindsay (Oligocene)				ca. 34[e]

The range of the "Triassic" ages obtained in this work is from 229.1 ± 1.8 to 196 ± 17 Ma; a mean age of 211 Ma (Late Triassic—Norian) has been assigned here

Key: MM GRD: *MM Granodiorite*; MM-P: *MM Porphyry*; QTZ-P: *Quartz-Porphyry*; DAC-P: *Dacitic Porphyry*; HRNB-P: *Hornblende Porphyry*, GRD ESTE-RT: *East Granodiorite*, Radomiro Tomic (RT) Mine; E-P RT: *East Porphyry*, RT Mine; E-P CHU: *East Porphyry*, Chuquicamata Mine; B-P CHU: *Banco Porphyry*, Chuquicamata Mine

[a]Due to the presence of inherited zircons and oscillatory zoning, the U–Pb dates obtained have a large uncertainty

[b]Eocene and Oligocene ages are assigned by correlation with dated units. The presence of inherited zircons and oscillatory zoning lead to large uncertainty. The Eocene–Oligocene boundary of 33.9 Ma has been adopted (Intl. Chronostratigraphic Chart, ICS V 2017-2)

[c]Not dated; ages assigned by correlation. Dates for Este Granodiorite range from 231.4 ± 2.0 Ma to 233.1 ± 2.2 Ma (Barra et al. 2013)

[d]Eocene (ca. 35 Ma) age for *Este Porphyry*

[e]Oligocene (ca. 33.4 Ma) for *Banco Porphyry* in Chuquicamata from U–Pb studies (see text)

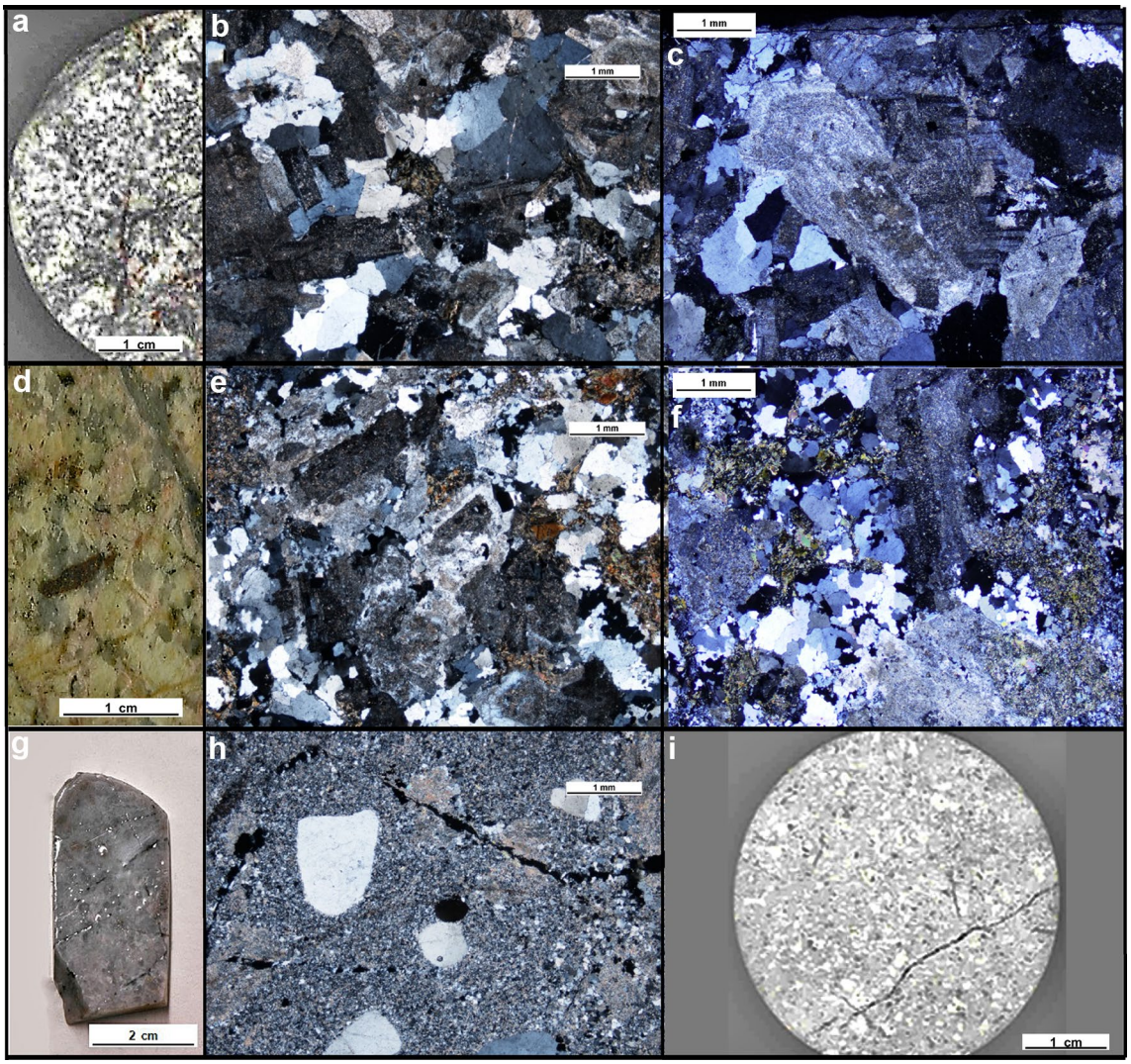

Fig. 4 Rock types within MMH. **a** Triassic MM granodiorite hand specimen; **b** Microphotograph of *MM Granodiorite* under crossed nicols; **c** Megacrysts of K-feldspar in MM granodiorite affected by potassic alteration; **d** Photograph of equigranular Eocene *MM Porphyry* in drillcore (from Proffett 2008); notice (near center) subhedral crystal of sphene (titanite) partially replaced by rutile and leucoxene; **e** *MM Porphyry* under crossed-polarized light; **f** *MM Porphyry* with potassic alteration and K-feldspar megacrysts; **g** Photograph of (wetted) Eocene *Quartz Porphyry*; **h** Microphotograph under crossed-polarized light of fine-grained *Quartz Porphyry* with distinctive quartz "eyes"; **i** Photograph of dacite dike (*Dacitic Porphyry*, Oligocene) in drillcore

Eocene–Oligocene rocks

The MM Porphyry Complex includes the voluminous *MM Porphyry*, the *Quartz Porphyry* and dikes of *Dacitic Porphyry*. The Chuqui Porphyry Complex includes the voluminous *Este Porphyry*, the minor *Oeste Porphyry*, and dike-like *Banco Porphyry*. Due to their similarity in chemistry, fluid inclusions mineralogy and age, they are tentatively interpreted as two fragments of the same complex separated by the West Fault (Zentilli et al. 2015).

The *MM Porphyry*, a porphyritic granodiorite of variable texture, is volumetrically the most important in the MMH deposit (Fig. 3). Phenocrysts of plagioclase (oligoclase–andesine, partially altered to albite), biotite and biotitized hornblende occur throughout the unit, within a matrix of anhedral interstitial quartz and K-feldspar. Sphene (titanite) megacrysts are conspicuous (Fig. 4d), commonly pseudomorphed by rutile or leucoxene. Some phases of the *MM Porphyry* are equigranular, and very similar in texture to the quartz-rich phases of the Triassic *MM Granodiorite*. Where potassic alteration has developed K-feldspar megacrysts in the *MM Granodiorite*, the rocks are easily confused (Fig. 4c, f). Only two samples were deemed adequate for dating. One zircon sample (ZMMH-89) yielded a U–Pb date of 35.03 ± 0.34 Ma by LA-ICP-MS. Zircons from the same sample yielded a non-concordant lower intercept date

Table 2 Geochemical analyses of samples in Table 1

Field no.	Rock unit	SiO_2	Al_2O_3	TiO_2	Fe_2O_3(t)	MgO	MnO	CaO	K_2O	Na_2O	P_2O_5	LOI
Units		%	%	%	%	%	%	%	%	%	%	%
Detection limit		0.01	0.01	0.001	0.01	0.01	0.001	0.01	0.01	0.01	0.01	
Analytical method		FUS-ICP	FUS-ICP	FUS-ICP	FUS-ICP	FUS-ICP	FUS-ICP	FUS-ICP	FUS-ICP	FUS-ICP	FUS-ICP	FUS-ICP
ZMMH-15	MM GRD	54.73	21.83	0.414	3.38	3.37	0.096	2.35	4.44	4.44	0.09	4.21
ZMMH-04	HRNB-P	64.77	15.58	0.326	2.8	1.5	0.54	1.57	5.67	0.09	0.14	4.76
ZMMH-50	MM GRD	64.81	16.24	0.381	5.37	2.37	0.313	0.3	5.23	0.04	0.13	3.73
ZMMH-23	MM GRD	66.48	17.2	0.358	3.18	2.8	0.205	0.16	4.85	0.09	0.09	3.78
ZMMH-163	MM GRD	66.64	15.21	0.375	3.3	1.56	0.086	2.42	2.33	4.25	0.07	2.99
ZMMH 10	MM GRD	67.1	15	0.382	3.53	1.4	0.201	1.97	2.19	5.09	0.1	3.39
ZMMH-14	MM GRD	68.36	15.98	0.407	1.98	1.78	0.055	2.19	3.26	4.47	0.12	2.22
ZMMH-20	MM GRD	69.95	15.55	0.374	3.35	0.51	0.012	0.08	4.46	0.08	0.07	3.78
ZMMH-17	MM GRD	71.57	14.8	0.343	2.55	0.75	0.017	0.18	4.59	0.09	0.1	3.04
ZMMH-18	MM GRD	72.46	16.36	0.409	3.57	0.05	0.006	0.06	1.77	0.09	0.06	4.49
ZMMH-91	MM GRD	70.14	12.08	0.289	1.19	1.31	0.19	2.16	7.47	0.24	0.04	4.55
ZMMH-88	MM-P	66.59	13.09	0.33	1.55	1.14	0.183	2.22	6.24	0.25	0.42	5.16
ZMMH-07	MM-P	67.73	15.42	0.315	2.02	0.89	0.219	1.83	5.54	2.9	0.15	3.61
ZMMH-21	MM-P	69.79	15.54	0.367	2.39	1.1	0.027	0.18	5.56	0.1	0.09	3.1
ZMMH-96	MM-P	70.28	14.79	0.336	1.63	0.38	0.187	0.38	5.89	2.74	0.06	2
ZMMH-81	MM-P	71.04	15.18	0.32	2.49	0.99	0.08	0.05	5.02	0.05	0.02	3.32
ZMMH-89	MM-P	72.33	11.64	0.201	2.02	0.85	0.321	1.33	6.13	0.1	0.04	4.13
ZMMH-97	QTZ-P	64.98	13.42	0.233	1.18	0.29	0.059	2.43	8.94	0.31	0.06	6.22
ZMMH-164	QTZ-P	65.25	14.6	0.206	2.08	0.8	0.726	1.26	9.2	0.21	0.06	3.92
ZMMH-11	QTZ-P	69.55	15.63	0.247	1.87	0.58	0.02	0.16	7.53	0.16	0.1	2.73
ZMMH-162	QTZ-P	76.94	15.32	0.42	0.94	0.04	0.006	0.12	0.27	0.13	0.12	4.64
ZMMH-13	QTZ-P	77.17	11.79	0.162	3.37	0.22	0.012	0.05	3.22	0.08	0.03	3.12
ZMMH-12	QTZ-P	79.01	12.71	0.166	1.02	0.36	0.015	0.05	3.82	0.09	0.04	1.97
ZMMH-76	DAC-P	59.24	14.78	0.281	8.56	0.62	1.753	0.12	4.29	0.05	0.04	7.98
ZMMH-09	DAC-P	65.17	14.57	0.347	3.45	1.04	1.89	0.23	8.16	0.14	0.12	4.47
ZMMH-66	DAC-P	68.13	13.97	0.417	5.92	0.22	0.014	0.12	3.02	0.06	0.17	5.69
ZMMH-67	DAC-P	74.9	11.77	0.28	3.38	0.28	0.026	0.27	2.89	0.04	0.09	4.35
ZMMH-04	HRNB-P	64.18	15.29	0.336	2.34	1.02	0.293	2.16	9.51	0.36	0.16	4.5
ZMMH-160	DIORITE	55.87	18.98	0.667	7.26	2.61	0.091	5.71	1.79	3.33	0.02	2.6
Z169-ME1	GRD ESTE-RT	57.51	19.84	0.367	3.76	1.81	0.021	3.25	2.09	6.57	0.06	2.81
Z170-ME2	E-P RT	67.25	16.26	0.355	3.02	0.82	0.032	3.21	2.61	4.51	0.12	0.97
Cu-2022	E-P CHU	68.65	16.18	0.276	2.49	0.61	0.03	2.87	3	4.68	0.09	0.34

Table 2 (continued)

Field no.	Rock unit	SiO_2	Al_2O_3	TiO_2	Fe_2O_3(t)	MgO	MnO	CaO	K_2O	Na_2O	P_2O_5	LOI
Units		%	%	%	%	%	%	%	%	%	%	%
Detection limit		0.01	0.01	0.001	0.01	0.01	0.001	0.01	0.01	0.01	0.01	
Analytical method		FUS-ICP	FUS-ICP	FUS-ICP	FUS-ICP	FUS-ICP	FUS-ICP	FUS-ICP	FUS-ICP	FUS-ICP	FUS-ICP	FUS-ICP
Cu-1333	P-B CHU	69.27	17.1	0.273	1.65	0.32	0.01	1.91	2.74	4.96	0.04	0.96

Field no.	Rock unit	Total	S	Total S	Au	Ag	As	Ba	Be	Bi	Br	Cd
Units		%	%	%	ppb	ppm	ppm	ppm	ppm	ppm	ppm	ppm
Detection limit			0.001	0.01	1	0.5	1	1	1	0.1	0.5	0.5
Analytical method			TD-ICP	IR	INAA	MULT INAA / TD-ICP	INAA	FUS-ICP	FUS-ICP	FUS-MS	INAA	TD-ICP
ZMMH-15	MM GRD	99.33	0.42	n/a	45	0.65	2	602	3	0.25	0.575	0.2
ZMMH-04	HRNB-P	97.75	1.48	n/a	3	5.3	1	790	2	0.6	1.1	30
ZMMH-50	MM GRD	98.92	0.9	0.89	12	3.2	< 1	1219	3	1.7	0.9	0.5
ZMMH-23	MM GRD	99.19	1.46	n/a	5	1.8	2	544	2	0.2	1.2	3.8
ZMMH-163	MM GRD	99.23	0.16	0.18	< 1	< 0.5	2	855	1	0.2	< 0.5	< 0.5
ZMMH 10	MM GRD	100.35	1.06	n/a	< 1	< 0.5	15	455	1	< 0.1	< 0.5	3.6
ZMMH-14	MM GRD	100.82	0.22	n/a	15	1.6	< 1	504	2	0.2	< 0.5	< 0.5
ZMMH-20	MM GRD	98.22	3.03	n/a	30	5.9	37	307	1	0.7	1.2	< 0.5
ZMMH-17	MM GRD	98.03	1.58	n/a	3	< 0.5	4	706	1	< 0.1	< 0.5	< 0.5
ZMMH-18	MM GRD	99.33	3.15	n/a	70	2.6	51	79	< 1	0.5	1.2	< 0.5
ZMMH-91	MM GRD	99.66	0.76	0.76	44	1.6	2	839	1	0.4	1.2	0.8
ZMMH-88	MM-P	97.17	0.8	0.8	168	10.5	2	581	2	0.4	0.8	< 0.5
ZMMH-07	MM-P	100.62	0.28	n/a	5	1.2	4	842	2	< 0.1	< 0.5	0.9
ZMMH-21	MM-P	98.24	0.92	n/a	9	1.4	118	404	2	< 0.1	1.3	< 0.5
ZMMH-96	MM-P	98.67	0.57	0.52	26	5.8	247	625	1	0.6	< 0.5	1.6
ZMMH-81	MM-P	98.56	1.44	1.37	47	3.3	6	292	2	0.9	0.8	< 0.5
ZMMH-89	MM-P	99.09	1.15	1.08	29	4.1	< 1	782	1	1.3	0.7	14
ZMMH-97	QTZ-P	98.12	1.78	1.48	46	7.4	< 1	807	1	1.1	1.1	0.9
ZMMH-164	QTZ-P	98.31	1.01	0.94	16	1.8	3	1718	1	0.1	0.9	5.4
ZMMH-11	QTZ-P	98.58	0.71	n/a	21	2.6	118	922	2	0.7	< 0.5	0.5
ZMMH-162	QTZ-P	98.94	0.96	0.89	< 1	< 0.5	23	183	< 1	< 0.1	1	< 0.5
ZMMH-13	QTZ-P	99.22	2.53	n/a	13	3	8	130	< 1	0.2	< 0.5	< 0.5
ZMMH-12	QTZ-P	99.25	0.36	n/a	4	0.9	12	253	1	0.1	< 0.5	< 0.5
ZMMH-76	DAC-P	97.72	1.6	1.55	< 1	1.6	18	833	2	0.5	0.6	5
ZMMH-09	DAC-P	99.59	1.69	n/a	< 1	0.8	12	1815	1	< 0.1	< 0.5	6.9

Table 2 (continued)

Field no.	Rock unit	Total	S	Total S	Au	Ag	As	Ba	Be	Bi	Br	Cd
Units		%	%	%	ppb	ppm	ppm	ppm	ppm	ppm	ppm	ppm
Detection limit			0.001	0.01	1	0.5	1	1	1	0.1	0.5	0.5
Analytical method			TD-ICP	IR	INAA	MULT INAA / TD-ICP	INAA	FUS-ICP	FUS-ICP	FUS-MS	INAA	TD-ICP
ZMMH-66	DAC-P	97.73	4.99	4.6	< 1	3.3	214	361	< 1	0.2	< 0.5	4.1
ZMMH-67	DAC-P	98.28	2.86	2.56	< 1	3.3	102	235	< 1	< 0.1	< 0.5	17.5
ZMMH-04	HRNB-P	100.15	1.57	n/a	14	6.8	< 1	1262	2	1	< 0.5	3.7
ZMMH-160	DIORITE	98.93	0.03	0.05	< 1	< 0.5	9	546	2	< 0.1	< 0.5	0.8
Z169-ME1	GRD ESTE-RT	98.09	0.24	0.25	14	< 0.5	< 1	87	1	0.6	0.7	< 0.5
Z170-ME2	E-P RT	99.15	0.04	0.07	< 1	< 0.5	< 1	843	2	< 0.1	0.9	< 0.5
Cu-2022	E-P CHU	99.22	0.04	n/a	< 1	< 0.5	2	791	2	< 0.1	< 0.5	< 0.5
Cu-1333	P-B CHU	99.23	0.16	n/a	< 1	< 0.5	9	790	2	< 0.1	0.9	< 0.5

Field no.	Rock unit	Co	Cr	Cs	Cu	Ga	Ga XRF	Ge	Hf	Hg	In	Ir
Units		ppm	ppm	ppm	ppm	ppm	ppm	ppm	ppm	ppm	ppm	ppb
Detection limit		0.1	0.5	0.1	1	1	5	0.5	0.1	1	0.1	1
Analytical method		INAA	INAA	FUS-MS	TD-ICP	FUS-MS	PPXRF	FUS-MS	FUS-MS	INAA	FUS-MS	INAA
ZMMH-15	MM GRD	8.25	10.8	11.55	4840	30	28.5	2.2	4			
ZMMH-04	HRNB-P	3.3	9.9	4.6	5220	18	23	1.4	3.1	< 1	< 0.1	< 1
ZMMH-50	MM GRD	2.9	2.3	5.1	8170	18	16	2.5	3.3	< 1	0.6	< 1
ZMMH-23	MM GRD	6.8	15.2	4	7030	19	20	1.6	3.1	< 1	0.3	< 1
ZMMH-163	MM GRD	9.8	12.1	7.7	11	16	15	1.4	2.9	< 1	< 0.1	< 1
ZMMH 10	MM GRD	12.1	12.3	7.2	33	15	15	0.9	3.2	< 1	< 0.1	< 1
ZMMH-14	MM GRD	4.2	13.1	3	3610	18	17	2.3	3.6	< 1	< 0.1	< 1
ZMMH-20	MM GRD	4	23.6	1.9	> 10000	21	20	1.9	3.5	< 1	< 0.1	< 1
ZMMH-17	MM GRD	8.1	13.4	2.2	7170	16	14	1.9	3.1	< 1	< 0.1	< 1
ZMMH-18	MM GRD	7.2	22.6	1.2	7100	9	8	1.8	3.5	< 1	< 0.1	< 1
ZMMH-91	MM GRD	2	9.3	2.7	4780	14	12	2.3	2.4	< 1	< 0.1	< 1
ZMMH-88	MM-P	1.8	11.3	3.3	> 10000	16	13	2.2	2.6	< 1	< 0.1	< 1
ZMMH-07	MM-P	2.7	6.9	7	3310	17	17	1.8	3.7	< 1	< 0.1	< 1
ZMMH-21	MM-P	2.4	16.2	4.2	9470	15	13	4.4	3.1	< 1	0.1	< 1
ZMMH-96	MM-P	2	8.6	7.8	6610	15	12	2	2.7	< 1	< 0.1	< 1
ZMMH-81	MM-P	1.8	4.7	10	5740	22	21	1.7	3.4	< 1	0.1	< 1
ZMMH-89	MM-P	1.9	1.8	3.6	4450	14	15	1.5	2.1	< 1	< 0.1	< 1
ZMMH-97	QTZ-P	1.3	3.4	1.4	5230	15	13	2.5	2.4	< 1	< 0.1	< 1

Table 2 (continued)

Field no.	Rock unit	Co	Cr	Cs	Cu	Ga	Ga XRF	Ge	Hf	Hg	In	Ir
Units		ppm	ppm	ppm	ppm	ppm	ppm	ppm	ppm	ppm	ppm	ppb
Detection limit		0.1	0.5	0.1	1	1	5	0.5	0.1	1	0.1	1
Analytical method		INAA	INAA	FUS-MS	TD-ICP	FUS-MS	PPXRF	FUS-MS	FUS-MS	INAA	FUS-MS	INAA
ZMMH-164	QTZ-P	2.9	< 0.5	2.8	1660	18	16	1.4	2.6	< 1	< 0.1	< 1
ZMMH-11	QTZ-P	1.7	5.1	2.6	7510	17	15	4.3	3	< 1	< 0.1	< 1
ZMMH-162	QTZ-P	2	17.9	0.7	486	13	13	21.1	2.9	< 1	< 0.1	< 1
ZMMH-13	QTZ-P	3.3	10.5	5.1	6210	8	7	1.4	2.5	< 1	< 0.1	< 1
ZMMH-12	QTZ-P	0.8	7.7	0.9	2770	10	9	1.6	2.6	< 1	< 0.1	< 1
ZMMH-76	DAC-P	13.4	6.2	29.1	1440	18	17	2.5	3	< 1	0.5	< 1
ZMMH-09	DAC-P	8.3	12.7	6.9	118	14	14	3	2.9	< 1	< 0.1	< 1
ZMMH-66	DAC-P	18	8.4	24.4	1430	19	19	1.4	3.2	< 1	< 0.1	< 1
ZMMH-67	DAC-P	6.2	6.3	16.1	352	19	21	1.7	2.1	< 1	0.3	< 1
ZMMH-04	HRNB-P	2.2	6.7	2.3	5080	18	17	2.4	3	< 1	< 0.1	< 1
ZMMH-160	DIORITE	25.7	7.7	5.7	61	20	19	1.6	3.2	< 1	< 0.1	< 1
Z169-ME1	GRD ESTE-RT	10.3	9.7	4.4	3200	17	16	1.9	3.8	< 1	< 0.1	< 1
Z170-ME2	E-P RT	6.2	< 0.5	1.4	407	18	18	1.2	3.2	< 1	< 0.1	< 1
Cu-2022	E-P CHU	3.6	5.1	0.7	306	20	20	1.3	3.6	< 1	< 0.1	< 1
Cu-1333	P-B CHU	2.8	6	2.2	1560	22	21	1.6	3.2	< 1	< 0.1	< 1

Field no.	Rock unit	Mo	Nb	Ni	Pb	Pb XRF	Rb	Rb XRF	Sb	Sc	Se	Sn
Units		ppm	ppm	ppm	ppm	ppm	ppm	ppm	ppm	ppm	ppm	ppm
Detection limit		2	0.2	1	5	5	1	2	0.1	0.01	0.5	1
Analytical method		FUS-MS	FUS-MS	TD-ICP	TD-ICP	PPXRF	FUS-MS	PPXRF	INAA	INAA	INAA	FUS-MS
ZMMH-15	MM GRD	6	4.9	22	< 5	< 5	155	167	0.5	8.405	< 0.5	2.5
ZMMH-04	HRNB-P	67	7.6	11	1970	> 1000	227	197	0.8	3.68	< 0.5	2
ZMMH-50	MM GRD	22	5.2	5	< 5	< 5	241	250	0.8	4.36	< 0.5	2
ZMMH-23	MM GRD	2	5.7	20	< 5	9	159	173	0.4	7.8	< 0.5	2
ZMMH-163	MM GRD	< 2	13.1	16	13	19	45	51	0.7	7.56	< 0.5	1
ZMMH 10	MM GRD	< 2	4.5	19	369	346	58	54	0.8	6.72	< 0.5	1
ZMMH-14	MM GRD	2	5.6	16	< 5	8	78	85	0.3	8.12	< 0.5	2
ZMMH-20	MM GRD	20	65.1	11	< 5	9	114	122	0.4	7.87	5.4	6
ZMMH-17	MM GRD	> 100	3.7	23	< 5	< 5	133	144	0.3	7.57	< 0.5	4
ZMMH-18	MM GRD	18	4.7	17	14	13	46	52	1.5	7.4	5.5	11
ZMMH-91	MM GRD	> 100	3.9	14	43	47	167	173	2.2	6.06	< 0.5	2
ZMMH-88	MM-P	14	3.2	6	18	25	106	114	0.5	6.51	9.4	2

Table 2 (continued)

Field no.	Rock unit	Mo	Nb	Ni	Pb	Pb XRF	Rb	Rb XRF	Sb	Sc	Se	Sn
Units		ppm	ppm	ppm	ppm	ppm	ppm	ppm	ppm	ppm	ppm	ppm
Detection limit		2	0.2	1	5	5	1	2	0.1	0.01	0.5	1
Analytical method		FUS-MS	FUS-MS	TD-ICP	TD-ICP	PPXRF	FUS-MS	PPXRF	INAA	INAA	INAA	FUS-MS
ZMMH-07	MM-P	21	9.4	4	73	73	132	140	0.5	3.73	< 0.5	1
ZMMH-21	MM-P	60	3.7	6	5	< 5	220	237	2.2	5.75	< 0.5	3
ZMMH-96	MM-P	18	4.1	8	38	44	118	125	0.9	5.91	< 0.5	2
ZMMH-81	MM-P	23	4.5	4	114	124	236	253	0.6	5.12	< 0.5	5
ZMMH-89	MM-P	6	4.2	4	59	62	183	195	1.1	2.38	< 0.5	2
ZMMH-97	QTZ-P	13	6.1	4	9	14	157	165	0.3	2.48	< 0.5	3
ZMMH-164	QTZ-P	< 2	9.1	3	727	730	227	223	0.8	2.52	< 0.5	1
ZMMH-11	QTZ-P	> 100	6.3	6	12	14	191	207	2.5	2.93	< 0.5	3
ZMMH-162	QTZ-P	< 2	4.9	2	66	72	1	4	3.8	3.79	< 0.5	2
ZMMH-13	QTZ-P	27	6.9	5	6	< 5	92	99	1.5	2.43	3.8	17
ZMMH-12	QTZ-P	28	5.2	2	< 5	< 5	88	96	1.9	2.54	< 0.5	7
ZMMH-76	DAC-P	26	5.2	18	448	448	201	202	4.1	6.31	< 0.5	2
ZMMH-09	DAC-P	< 2	4	14	374	350	220	225	2.5	6.66	< 0.5	< 1
ZMMH-66	DAC-P	< 2	4.3	24	629	648	103	98	8.1	7.27	< 0.5	6
ZMMH-67	DAC-P	< 2	2.8	7	1330	> 1000	91	66	20.5	4.5	< 0.5	< 1
ZMMH-04	HRNB-P	16	8	5	76	73	231	244	0.6	3.88	< 0.5	2
ZMMH-160	DIORITE	< 2	10.7	15	15	25	56	61	0.5	11.4	< 0.5	2
Z169-ME1	GRD ESTE-RT	26	7.1	16	< 5	6	79	84	0.2	7.68	4.9	2
Z170-ME2	E-P RT	2	8.3	5	6	9	67	78	< 0.1	4.41	< 0.5	1
Cu-2022	E-P CHU	< 2	9.8	4	8	8	66	76	< 0.1	3.19	< 0.5	1
Cu-1333	P-B CHU	< 2	5.7	3	5	10	69	79	0.3	2.95	< 0.5	2

Field no.	Rock unit	Sr	Ta	Th	U	V	W	Y	Zn	Zr
Units		ppm	ppm	ppm	ppm	ppm	ppm	ppm	ppm	ppm
Detection limit		2	0.01	0.05	0.01	5	1	1	1	1
Analytical method		FUS-ICP	FUS-MS	FUS-MS	FUS-MS	FUS-ICP	INAA	FUS-ICP	TD-ICP	FUS-MS
ZMMH-15	MM GRD	416.5	0.505	5.83	1.865	132.5	< 1	13	46.5	146.5
ZMMH-04	HRNB-P	106	0.52	5.88	2.17	45	9	7	6210	111
ZMMH-50	MM GRD	58	0.47	4.38	0.92	57	14	6	291	143
ZMMH-23	MM GRD	12	0.39	4.77	1.35	66	15	9	1250	116
ZMMH-163	MM GRD	484	0.35	5.33	0.91	62	< 1	9	66	124
ZMMH 10	MM GRD	207	0.28	4.17	0.73	63	< 1	5	730	120

Table 2 (continued)

Field no.	Rock unit	Sr	Ta	Th	U	V	W	Y	Zn	Zr
Units		ppm	ppm	ppm	ppm	ppm	ppm	ppm	ppm	ppm
Detection limit		2	0.01	0.05	0.01	5	1	1	1	1
Analytical method		FUS-ICP	FUS-MS	FUS-MS	FUS-MS	FUS-ICP	INAA	FUS-ICP	TD-ICP	FUS-MS
ZMMH-14	MM GRD	370	0.32	4.46	1.04	75	4	8	55	139
ZMMH-20	MM GRD	168	58.4	4.45	3.57	70	15	9	35	130
ZMMH-17	MM GRD	26	0.31	3.5	1.12	73	13	6	21	112
ZMMH-18	MM GRD	214	0.31	4.91	0.98	85	17	7	16	133
ZMMH-91	MM GRD	157	0.43	4.23	3.02	61	6	6	138	98
ZMMH-88	MM-P	117	0.26	5.02	1.34	64	6	22	57	114
ZMMH-07	MM-P	244	0.7	9.68	1.7	41	5	6	227	126
ZMMH-21	MM-P	37	0.23	3.84	0.91	54	17	5	98	122
ZMMH-96	MM-P	133	0.41	5.8	1.81	43	10	9	430	113
ZMMH-81	MM-P	240	0.4	4.97	1.8	47	36	10	54	145
ZMMH-89	MM-P	165	0.37	4.49	0.95	30	9	4	3130	88
ZMMH-97	QTZ-P	252	0.5	5.32	0.92	29	10	5	250	104
ZMMH-164	QTZ-P	231	0.53	5.64	2.07	23	9	6	1230	105
ZMMH-11	QTZ-P	132	0.43	4.14	1.97	27	13	5	93	110
ZMMH-162	QTZ-P	687	0.34	4.95	1.7	66	38	5	3	122
ZMMH-13	QTZ-P	56	0.47	5.11	0.96	36	18	7	22	80
ZMMH-12	QTZ-P	58	0.48	5.23	0.91	22	11	7	21	84
ZMMH-76	DAC-P	188	0.49	6.31	1.68	43	9	8	1300	128
ZMMH-09	DAC-P	137	0.31	4.36	1.34	54	13	9	1660	106
ZMMH-66	DAC-P	561	0.36	4.15	3.01	75	34	5	262	144
ZMMH-67	DAC-P	464	0.27	3.31	1.77	57	15	3	2470	92
ZMMH-04	HRNB-P	307	0.54	5.48	0.95	46	10	6	906	107
ZMMH-160	DIORITE	418	0.48	6.48	1.47	241	< 1	17	72	130
Z169-ME1	GRD ESTE-RT	232	0.65	9.51	2.01	53	6	8	24	146
Z170-ME2	E-P RT	679	0.54	12.2	2.13	50	< 1	7	28	133
Cu-2022	E-P CHU	647	0.61	7.22	2.72	33	< 1	5	121	122
Cu-1333	P-B CHU	640	0.38	4.46	5.06	27	8	11	343	115

Key as in Table 1

FUS-ICP lithium metaborate/tetraborate fusion followed by ICP, *TD-ICP* total digestion followed by ICP, *IR* infrared, *INAA* instrumental neutron activation analysis, *MULT* multiple methods listed used depending on concentration, *FUS-MS* total fusion followed by mass spectrometry, *PP-XRF* pressed pellet followed by X-ray fluorescence

Table 3 Rare earth analyses

Sample	Rock unit	La	Ce	Pr	Nd	Sm	Eu	Gd	Tb	Dy	Ho	Er	Tl	Tm	Yb	Lu
Units		ppm	ppm	ppm	ppm	ppm	ppm	ppm	ppm	ppm	ppm	ppm	ppm	ppm	ppm	ppm
Detection limit		0.05	0.05	0.01	0.05	0.01	0.005	0.01	0.01	0.01	0.01	0.01	0.05	0.005	0.01	0.002
Method		FUS-MS = Total Fusion followed by mass spectrometry														
ZMMH-15	MM GRD	34.7	59	5.99	20.6	3.78	1.14	3.09	0.46	2.44	0.5	1.39	1	0.22	1.45	0.22
ZMMH-05	HRNB-P	24.5	45.6	4.34	15.1	2.44	0.8	1.56	0.21	1.12	0.21	0.63	1.94	0.1	0.64	0.11
ZMMH-50	MM GRD	24.6	41.7	4.48	15.2	2.49	0.79	1.82	0.24	1.21	0.23	0.66	1.6	0.1	0.64	0.09
ZMMH-23	MM GRD	17.4	33.3	3.22	11.8	2.09	0.4	1.72	0.28	1.57	0.31	0.91	1.22	0.15	1.04	0.18
ZMMH-163	MM GRD	31.9	60.3	6.5	22.5	3.65	0.99	2.71	0.35	1.79	0.33	0.9	0.4	0.13	0.83	0.13
ZMMH 10	MM GRD	17.3	32.2	3.15	11.5	1.88	0.58	1.36	0.2	1.1	0.22	0.63	0.58	0.1	0.65	0.11
ZMMH-14	MM GRD	17.1	32.4	3.16	11.9	2.14	0.62	1.64	0.26	1.45	0.29	0.85	0.37	0.13	0.91	0.16
ZMMH-20	MM GRD	19	35.4	3.35	11.6	2.01	0.5	1.66	0.24	1.46	0.28	0.83	0.75	0.13	0.9	0.15
ZMMH-17	MM GRD	12.6	24.9	2.47	8.94	1.48	0.33	1.24	0.2	1.21	0.25	0.76	0.97	0.12	0.81	0.14
ZMMH-18	MM GRD	20.7	40	3.9	14	2.56	0.63	1.75	0.23	1.3	0.27	0.89	0.36	0.15	1.06	0.19
ZMMH-91	MM GRD	8.38	16.4	1.86	6.8	1.29	0.42	1.13	0.17	0.93	0.19	0.55	1.7	0.09	0.56	0.09
ZMMH-88	MM-P	14.2	31.7	4	16.3	3.92	0.76	3.99	0.65	3.72	0.78	2.15	1	0.34	2.01	0.3
ZMMH-07	MM-P	25.7	47.7	4.69	16.5	2.65	0.67	1.76	0.24	1.27	0.24	0.7	0.95	0.11	0.79	0.13
ZMMH-21	MM-P	16.4	29.7	2.89	10.4	1.84	0.58	1.42	0.21	1.13	0.23	0.68	1.19	0.1	0.72	0.12
ZMMH-96	MM-P	34.7	68.1	7.05	22.3	3.36	0.66	2.2	0.29	1.62	0.35	1.08	1.1	0.18	1.12	0.17
ZMMH-81	MM-P	22	40.3	4.3	14.6	2.61	0.7	2.17	0.31	1.73	0.34	0.97	2	0.15	1.01	0.15
ZMMH-89	MM-P	7.85	14.9	1.67	6	1.12	0.28	0.88	0.13	0.67	0.13	0.38	2.2	0.07	0.43	0.06
ZMMH-97	QTZ-P	9.68	18.5	2.13	7.62	1.39	0.42	1.08	0.15	0.81	0.16	0.47	1.1	0.08	0.52	0.09
ZMMH-164	QTZ-P	20.3	36.8	3.87	13.3	1.99	0.56	1.44	0.18	0.87	0.16	0.46	2.6	0.07	0.48	0.07
ZMMH-11	QTZ-P	17.1	32.8	3.3	11.6	1.98	0.53	1.3	0.18	1	0.19	0.55	1.18	0.09	0.64	0.11
ZMMH-162	QTZ-P	23	42.7	4.66	16.3	2.8	0.76	1.92	0.2	0.83	0.15	0.47	< 0.05	0.08	0.62	0.11
ZMMH-13	QTZ-P	19	36.2	3.42	11.4	1.76	0.38	1.14	0.18	1.13	0.24	0.75	0.65	0.12	0.82	0.13
ZMMH-12	QTZ-P	15.6	28.6	2.69	9.37	1.59	0.44	1.34	0.21	1.19	0.24	0.74	0.49	0.12	0.84	0.14
ZMMH-76	DAC-P	23.2	41.8	4.38	14.5	2.28	0.53	1.88	0.28	1.6	0.33	0.98	1.5	0.16	1.1	0.16
ZMMH-09	DAC-P	18.4	35.4	3.49	12.3	2.17	0.73	1.65	0.25	1.47	0.29	0.87	3.12	0.14	0.95	0.16
ZMMH-66	DAC-P	18.2	35	3.82	13.8	2.82	1.02	2.62	0.3	1.06	0.2	0.68	1.5	0.12	0.94	0.15
ZMMH-67	DAC-P	9.05	15.4	1.6	5.5	1.15	0.35	0.88	0.08	0.4	0.09	0.34	1.3	0.07	0.52	0.09
ZMMH-04	HRNB-P	21.4	41.4	4.21	15.5	2.59	0.64	1.81	0.24	1.23	0.23	0.64	1.56	0.1	0.64	0.11
ZMMH-160	DIORITE	22.8	47	5.52	20	3.99	1.11	3.5	0.59	3.34	0.7	1.99	0.3	0.33	2.11	0.31
Z169-ME1	GRD ESTE-RT	18.9	35.2	3.98	13.6	2.43	0.59	1.98	0.3	1.61	0.32	0.94	0.4	0.16	1.15	0.17
Z170-ME2	E-P RT	23.9	44.5	4.97	17.5	2.87	0.76	2.04	0.26	1.33	0.25	0.69	0.3	0.11	0.68	0.1
Cu-2022	E-P CHU	19.5	37.5	3.77	13.6	2.32	0.61	1.55	0.2	1.07	0.21	0.61	0.12	0.1	0.67	0.12
Cu-1333	P-B CHU	14.1	26.2	2.43	8.58	1.57	0.54	1.42	0.28	1.8	0.36	1.05	0.21	0.17	1.14	0.19

Key as in Table 1

of ca. 35 Ma by TIMS (Zentilli 2012). Therefore, the *MM Porphyry* is Eocene in age.

The *MM Quartz Porphyry* intrudes the *MM Porphyry*, and is relatively abundant deep in the deposit (~ 1400 m; Fig. 3); it is a very fine-grained rock with abundant quartz "eyes" (spheroidal quartz crystals) of more than 6 mm, in an aplitic groundmass of quartz and sericite (Fig. 4g, h). There are zoned feldspar phenocrysts (0.5–4 mm) which are completely sericitized (blue-green sericite); there are K-feldspar megacrysts that could be primary or due to alteration, as well as anhydrite. A mineralized sample of *MM Quartz Porphyry* (ZMMH-97, Table 1) was dated by TIMS on zircon at 35.3 ± 3.5 Ma (Zentilli et al. 2015), and Boric et al. (2009) reported a U–Pb date of 35.5 ± 0.6 Ma for a sample of the same unit. Therefore, based on available data, the *MM Quartz Porphyry* is considered Eocene in age.

Dacitic Porphyry at MMH. Narrow aphanitic dacite dikes, with light color, aphanitic texture (Fig. 4i) and conspicuous brittle fracture, are relatively abundant in the upper levels of the deposit; they are in general younger than the

other MM porphyries and characterized by an assemblage of plagioclase and quartz and small amounts of hornblende; they typically contain disseminated pyrite. In a few places, where the rock has abundant feldspar megacrysts, it has been mapped as "*Feldspar Porphyry*". One sample of *MM Dacitic Porphyry* with abundant feldspar phenocrysts yielded a date of 33.7 ± 0.8 Ma (U–Pb on zircon, TIMS), hence Early Oligocene or latest Eocene (The Eocene–Oligocene boundary is given as 33.9 Ma; Cohen et al. 2017). Rivera et al. (2012) indicate that a few dacitic bodies within the MMH deposit are Triassic in age (one dated by U–Pb zircon at 223 ± 3.7 Ma by Tobey 2005), but the peculiar geochemistry of the samples analyzed in this study (see below) suggests they postdate the Cu and Mo mineralization.

The *Este Porphyry* of the Chuqui Porphyry Complex is the largest and oldest of the Eocene intrusions (Ossandón et al. 2001; Campbell et al. 2006). It has an inhomogeneous hypidiomorphic-granular texture with euhedral plagioclase (> 2 mm), biotite, biotitized hornblende and common K-feldspar in a matrix of quartz, K-feldspar, and biotite. There is no euhedral quartz, but generally elongated polycrystalline and strained quartz blebs. Este Porphyry is everywhere affected by potassic alteration, the original oligoclase–andesine is presently albite, and hornblende and titanite are replaced by biotite and rutile, respectively (Arnott 2003). It has been dated beyond the zone of pervasive potassic alteration by U–Pb at ca. 36 Ma (Ossandón et al. 2001; Proffett and Dilles 2007; Rivera et al. 2012), and Ballard et al. (2001) indicate an age of 34.6 ± 0.2 Ma within the mine. Two representative (and particularly unaltered) samples of *Este Porphyry* were chemically analyzed, one from Chuquicamata (Cu-2022) and another from RT mine (Z170-ME2; Table 1); these specific samples were not dated in the study, but by correlation in the mine, their age is ca. 35 Ma.

The *Oeste Porphyry* is a smaller body in the western part of the Chuquicamata deposit, and has smaller plagioclase phenocrysts (< 2 mm) and an abundance of quartz "eyes" in a groundmass of much finer equigranular quartz. The age of the *Oeste Porphyry* is 33.5 ± 0.2 Ma (Ballard et al. 2001), hence Oligocene (Cohen et al. 2017).

Dike-like bodies of *Banco Porphyry* occur in the northeastern part of the Chuquicamata pit (Ossandón et al. 2001). It is finer grained than Este Porphyry, and characterized by porphyritic plagioclase in an aphanitic (and finely porphyritic) groundmass. It has an assemblage of oligoclase, K-feldspar, quartz, biotite and rutile. The *Banco Porphyry* has preserved igneous intermediate plagioclase (oligoclase), in contrast with potassic altered *Este Porphyry*, which contains only secondary albite (Arnott and Zentilli 2003). *Banco Porphyry* was dated by U–Pb on zircon at 33.3 ± 0.3 Ma (Ballard et al. 2001); the Ar–Ar age of potassic alteration (biotite and K-feldspar) is 33.4 ± 0.3 Ma (Reynolds et al. 1998); therefore Oligocene (Cohen et al. 2017). One unaltered, representative sample of *Banco Porphyry* has been chemically analyzed for this study (Cu-1333, Table 1), but no date is available for this specific sample.

Geochemistry

The results for geochemical analyses are shown in Tables 2 and 3. Within a mineralized porphyry there are no unaltered (fresh) rocks; a measure of this alteration is the content of volatiles (Loss on Ignition; LOI), substantial in some samples (up to 8%). For plotting purposes, the analyses in Tables 2 and 3 have been recalculated volatile-free; this adjustment may amplify somewhat the content of some trace elements. Most samples in MMH and Chuquicamata are highly silicic, with SiO_2 content (Fig. 4) between 65 and 79 wt%, thus granodiorite to granite, the intrusive equivalent of dacite, rhyodacite and rhyolite. A few of the rocks are diorite/andesite. Due to hydrothermal alteration (potassic, sericitic, chloritic), the content of the mobile alkalis may not reflect the original composition; the rocks are calc-alkaline according to a SiO_2 vs. K_2O diagram by Peccerillo and Taylor (1976). Minor and trace elements such as Ti and Zr sited in refractory minerals are more likely to have been relatively immobile during alteration processes. On discriminant diagrams by Winchester and Floyd (1977) the MMH rocks are rhyodacite-dacite (granodiorite) and rhyolite (granite). Figure 5 indicates that based on Nb, Y, Zr and Ti, in diagrams by Winchester and Floyd (1977) and Pearce (1996), half the rocks qualify as trachyandesites. It is evident that the composition of Triassic and Eocene–Oligocene intrusives at MMH and Chuquicamata overlap in composition. For comparison, Fig. 5a shows the contrast between the composition of Triassic (this study) and Jurassic igneous rocks [volcanic and intrusive; (dotted line; data from Oliveros et al. 2007)] that occur along the coastal belt (Fig. 1). One sample of *MM Porphyry* (ZMMH-88) appears anomalous (Fig. 5b, c); it is highly mineralized with Cu, Ag, Se, and has among the lowest Nb (3.3 ppm; avg. 7.8); it also has the highest Y (22 ppm vs. avg. 7.7) and highest P_2O_5 (0.42%; vs. avg. 0.09); its composition has been affected by hydrothermal alteration.

One objective of the research in MMH was to look for effective ways to distinguish between Triassic and Eocene intrusives (Zentilli 2012). After multiple attempts, a plot of Ni vs. Fe_2O_3(total) (Fig. 6) represents the most convincing method to distinguish Triassic *MM Granodiorite* from the Eocene–Oligocene MM Porphyry Complex, at least the voluminous *MM Porphyry* and *Quartz Porphyry*, plus the *Este* and *Banco Porphyries* of Chuqui. However, the *Dacitic Porphyry*, although Oligocene in age, plots in the field of Triassic intrusives. This discrepancy does not represent a problem, because the *Dacitic Porphyry* is a significantly different rock (Fig. 4i), as demonstrated in Fig. 7. *Dacitic*

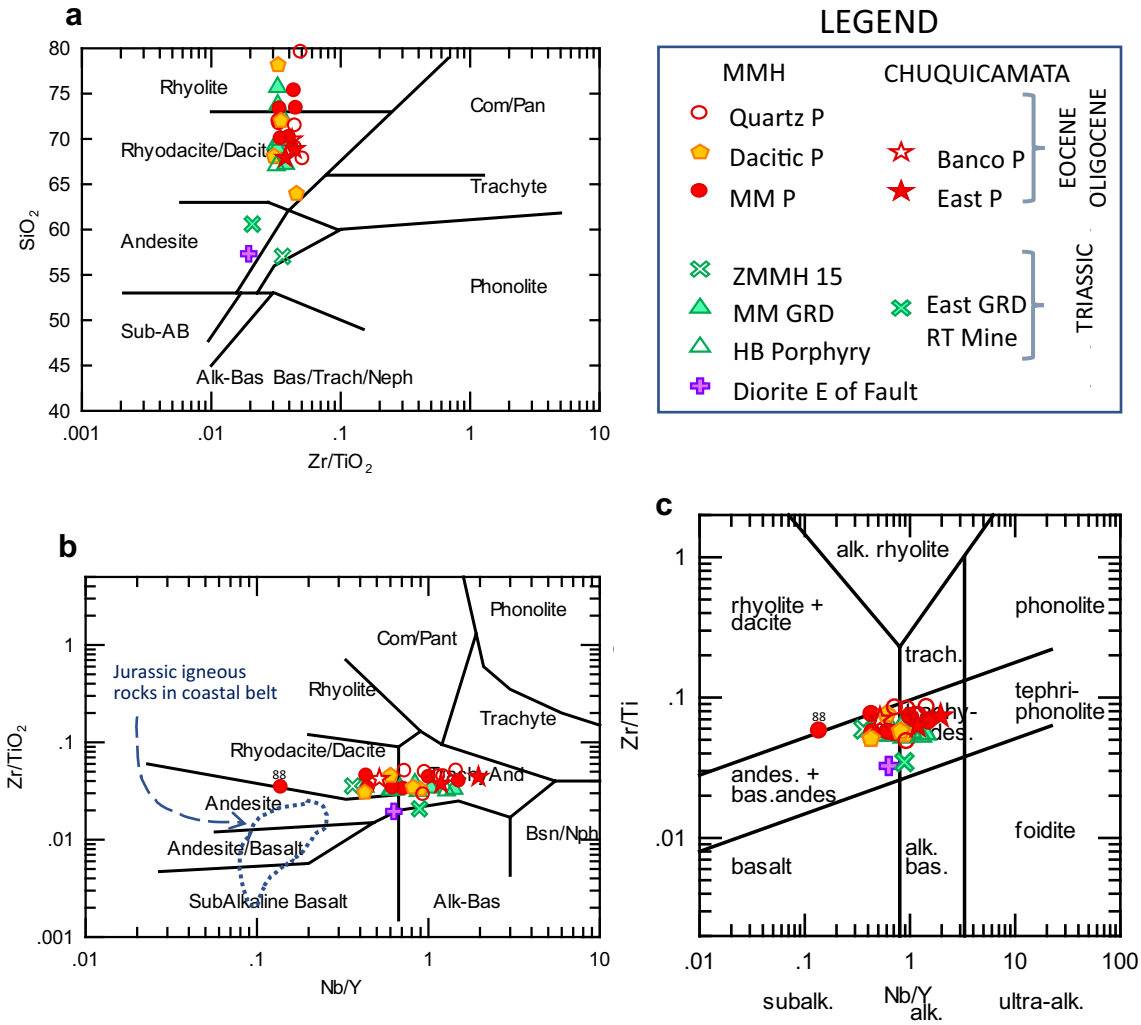

Fig. 5 Comparison of Triassic and Eocene–Oligocene rocks from MMH and Chuquicamata. In **a** SiO_2 vs. Zr/TiO_2 and **b** Nb/Y vs. Zr/TiO_2 diagrams from Winchester and Floyd (1977) and **c** Nb/Y vs. Zr/Ti after Pearce (1996). Most rocks are granodiorite, the intrusive equivalents of rhyodacite to trachyandesite or andesite. Hydrothermal alteration has added SiO_2 and LOI, but analyses have been recalculated volatile-free for all plots; one sample of MM Porphyry (MMH-88; Table 1) is anomalously high in Y, also the most hydrothermally altered (> 5% LOI and high in P_2O_5). Dashed line: Jurassic intrusive and volcanic rocks in the coastal belt of northern Chile (18.5°S to 34°S, from Oliveros et al. 2007). See text for "Discussion"

Porphyry is volumetrically minor in the deposit and relatively barren. Although indistinguishable from the other intrusives in terms of SiO_2, Al_2O_3, and TiO_2 (Fig. 7a, c), *Dacitic Porphyry* is notably enriched in Fe and S and LOI (Fig. 7 b) and Ni (Fig. 6), which leads to the interpretation that these elements may be contained in ubiquitous pyrite. The *Dacitic Porphyry* is also anomalously enriched in Cs, but depleted in Cu and Mo (Fig. 7e, f), suggesting that it was emplaced after the main phases of economic mineralization for those metals.

Further demonstrating the similarity between Triassic and Eocene–Oligocene intrusives, Fig. 8a, b shows that in terms of Ga/Al and Zr, and Yb + Ta and Rb, the rocks are tightly clustered in the field of I and S granitoids and straddling the fields Volcanic Arc and Collision granitoids, respectively (Pearce et al. 1984). It is probable that the Rb content has been increased by potassic and sericitic (phyllic) alteration. REE patterns (Fig. 8c; chondrite normalized after Sun and McDonough 1989) confirm the resemblance between Triassic and Eocene–Oligocene intrusives in the MMH mine. The "hockey stick" pattern and the lack of Eu anomaly is suggestive of amphibole fractionation of oxidized magmas, and possibly residual garnet in the source region, typical of calc-alkaline magmas of Andean type margins. In contrast, Jurassic and Early Cretaceous volcanic rocks that outcrop on the coastal belt at latitude 27°S (Fig. 1) show a moderate enrichment in light REE (LREE) and only small fractionation of heavy REE (HREE), features which are typical of

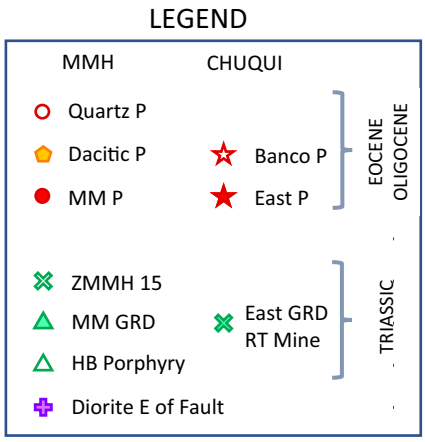

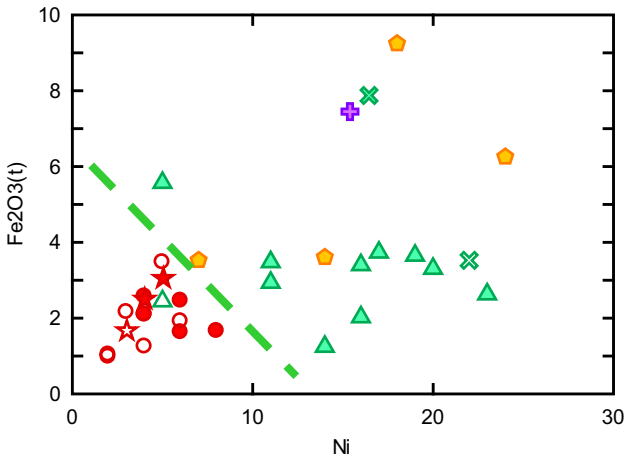

Fig. 6 Volatile-free plot Ni vs. Fe_2O_3 (total) that allows to distinguish Triassic and Eocene–Oligocene intrusions in MMH and Chuquicamata. Triassic rocks (green) in MMH and Chuquicamata have relatively higher Ni and Fe than the Tertiary intrusives. The *Dacitic Porphyry* of MMH overlaps in terms of these elements, but this rock type is very easy to recognize in the field (Fig. 4i). Legend as in Fig. 5

calc-alkaline rocks of island arcs with minimal crustal thickness (e.g., Dostal et al. 1977).

Figure 9a, b are spider diagrams of rock/primitive mantle normalized trace element plot after Sun and McDonough (1989). The similarity between Triassic and Eocene–Oligocene rocks analyzed is noteworthy; both have arc signatures.

A surprising result of this study was the finding that the MMH and Chuquicamata intrusives of Triassic and Eocene–Oligocene age are relatively low in Th and U (Fig. 10a) and TiO_2 (Fig. 10b) when compared with other suites of the region (data from Ballard 2001). However, the Th/U ratio is common to all rocks (average 3.6) suggesting the values may be primary. At El Abra (mine north of Radomiro Tomic in Fig. 1), the *El Abra Mine Porphyry* and *South Granodiorite* of Eocene age (Campbell et al. 2006) show similarities with those from the Triassic *MM Granodiorite* and the Eocene *MM Porphyry*, although some rocks from the Fortuna–Los Picos complexes (Eocene; 37–43.7 Ma; Tomlinson and Blanco 2008) show minor overlap. The triangular plot U + Th − TiO_2 − Zr (Fig. 11a) shows the coincidence of Triassic and Eocene–Oligocene rocks at MMH and Chuquicamata, and similarity with mineralized rocks at El Abra–Los Picos complexes. Figure 11b is a plot U + Th (in ppm), TiO_2 and P_2O_5 (in wt %), which shows the anomalously high content of P_2O_5 in sample ZMMH 88, which is highly altered (5.16 wt% LOI) and yields normative apatite; the same sample is anomalously rich in Y and plots off the general suite in Fig. 5b, c.

Discussion

Chemical similarity of Triassic and Eocene–Oligocene intrusives

The remarkable chemical similarity between Triassic and Eocene–Oligocene intrusives within the MMH, (and Chuquicamata and RT) deposits explains the difficulty that generations of geologists have encountered distinguishing them in the mine and in core. The rocks show textural variations from place to place and probably represent multiple phases. Hydrothermal alteration of the Triassic *MM Granodiorite*, can develop K-feldspar megacrysts that mimic porphyry textures and the similar phases that are found in MM Porphyry Complex rocks (Fig. 4c, f). The best chemical discriminant is the relatively higher Fe and Ni content of the Triassic granodiorite (Fig. 6), and these elements would be easy to add to routine analysis of mine samples. Although the *Dacitic Porphyry* overlaps in composition in terms of those elements, its aphanitic texture (Fig. 4i), brittle properties and occurrence as narrow dikes make it easier to recognize.

The *Dacitic Porphyry*, besides being rich in Fe and Ni is also quite distinct in its relatively high content of Cs, Cd, Pb, In, Zn, and S, compared to the other intrusives, but is not enriched in economically important Mo, Cu, Ag nor Au. The *Dacitic Porphyry* of MMH contains an order of magnitude more: 7–31 ppm (avg. 20.3 ppm) than the Cs content of volcanic and intrusive rocks, which is generally less tan 1 ppm (Horstman 1957); other MMH rocks contain less than 10 ppm Cs (as do Tertiary igneous rocks from El Abra–Pajonal and Fortuna–Los Picos Complexes in the Domeyko Cordillera; avg. 5.2 ppm; Ballard 2001). It is likely that the *Dacitic Porphyry* dikes were emplaced late in the history of the deposit, certainly after the formation of high-grade hydrothermal breccias rich in Cu. This is consistent with the U–Pb zircon age obtained in this study (Early Oligocene).

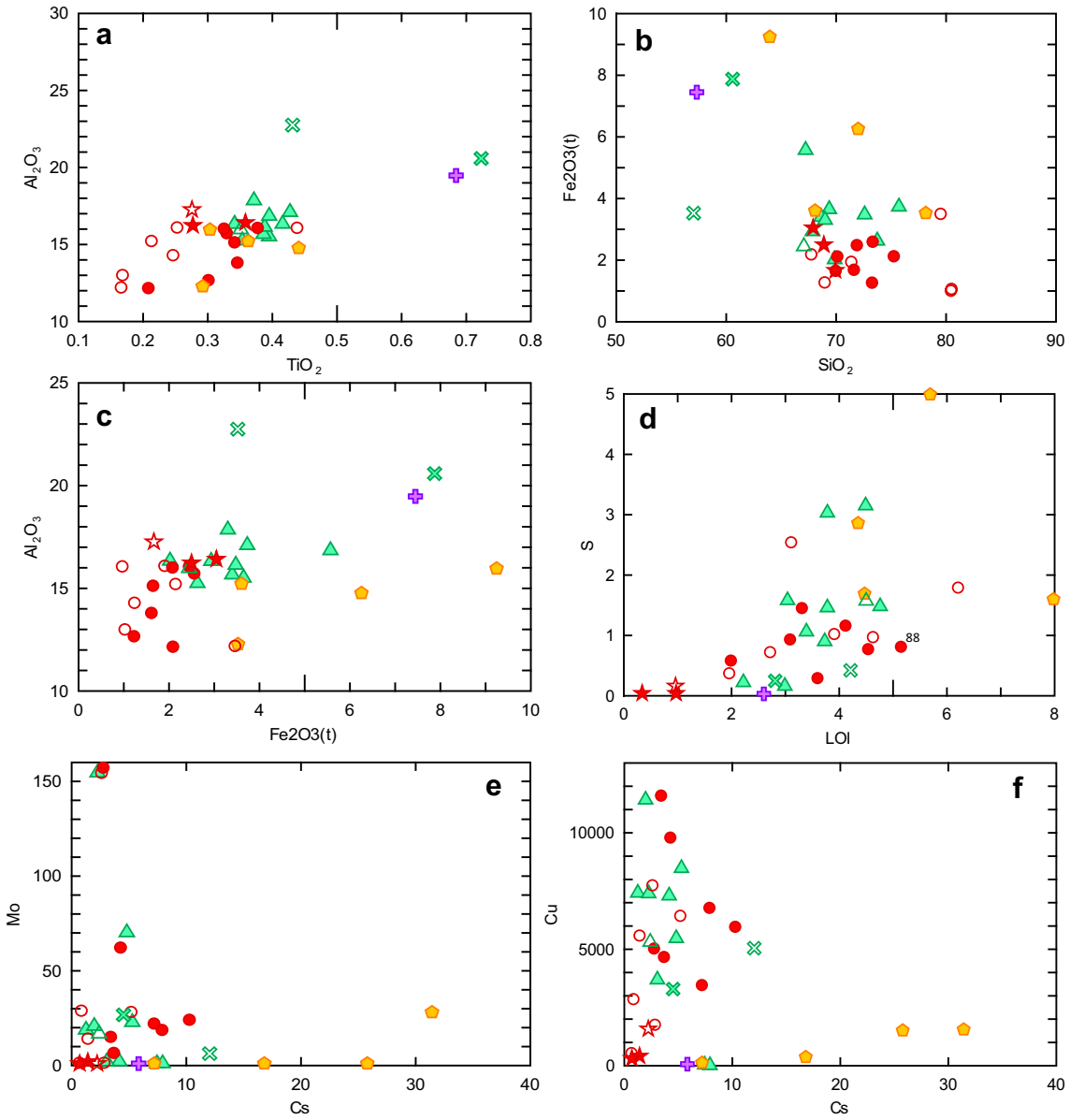

Fig. 7 Plots attempting to show differences between rocks types at MMH. **a, b** Triassic *MM Granodiorite* (green) is slightly enriched in Al_2O_3 and Fe_2O_3 (tot), but very close in composition to Eocene–Oligocene porphyries in terms of Al_2O_3 and SiO_2. **c** The Triassic *Este Granodiorite* of RT mine and an undated diorite sampled east of the West Fault within MMH have more TiO_2 and Fe_2O_3 than the Triassic *MM Granodiorite*. **d** All rocks show similar patterns of alteration with increases in S and LOI, but the *Dacitic Porphyry* (Oligocene) is most affected. **e, f** Plots to show how the Oligocene *Dacitic Porphyry* of MMH is generally enriched in Cs, but not affected by pervasive Mo and Cu mineralization as are the other rocks. All plots with data recalculated volatile-free. Legend as in Fig. 5

Despite the variable states of alteration of the samples, Triassic and Eocene–Oligocene rocks in MMH plot in tight groups, suggesting that the trace elements used in the various diagrams are contained in relatively refractory minerals, such as titanite and zircon. Case in point are the diagrams in Figs. 8a, b, and 9. Especially the REE (Fig. 8c) show a considerable overlap in a composition/chondrite diagram by Sun and McDonough (1989). From isotopic data for Pb, Sr, Nd, and Os in ores it appears the Chuquicamata magmas had mantle affinities and negligible crustal contamination (Zentilli et al. 1988, 2015; Maksaev 1990; Tosdal et al. 1999; Mathur et al. 2000). These results contrast with the statement of Kramer and Ehrlichmann (1996) that in northern Chile between 20° and 26°30′S, Triassic and part of Lower Jurassic precursors of intermediate to acid character have predominant crustal sources. The parallel in geochemistry or Triassic intrusives and Eocene–Oligocene porphyries that occur in the exact same location in the crust

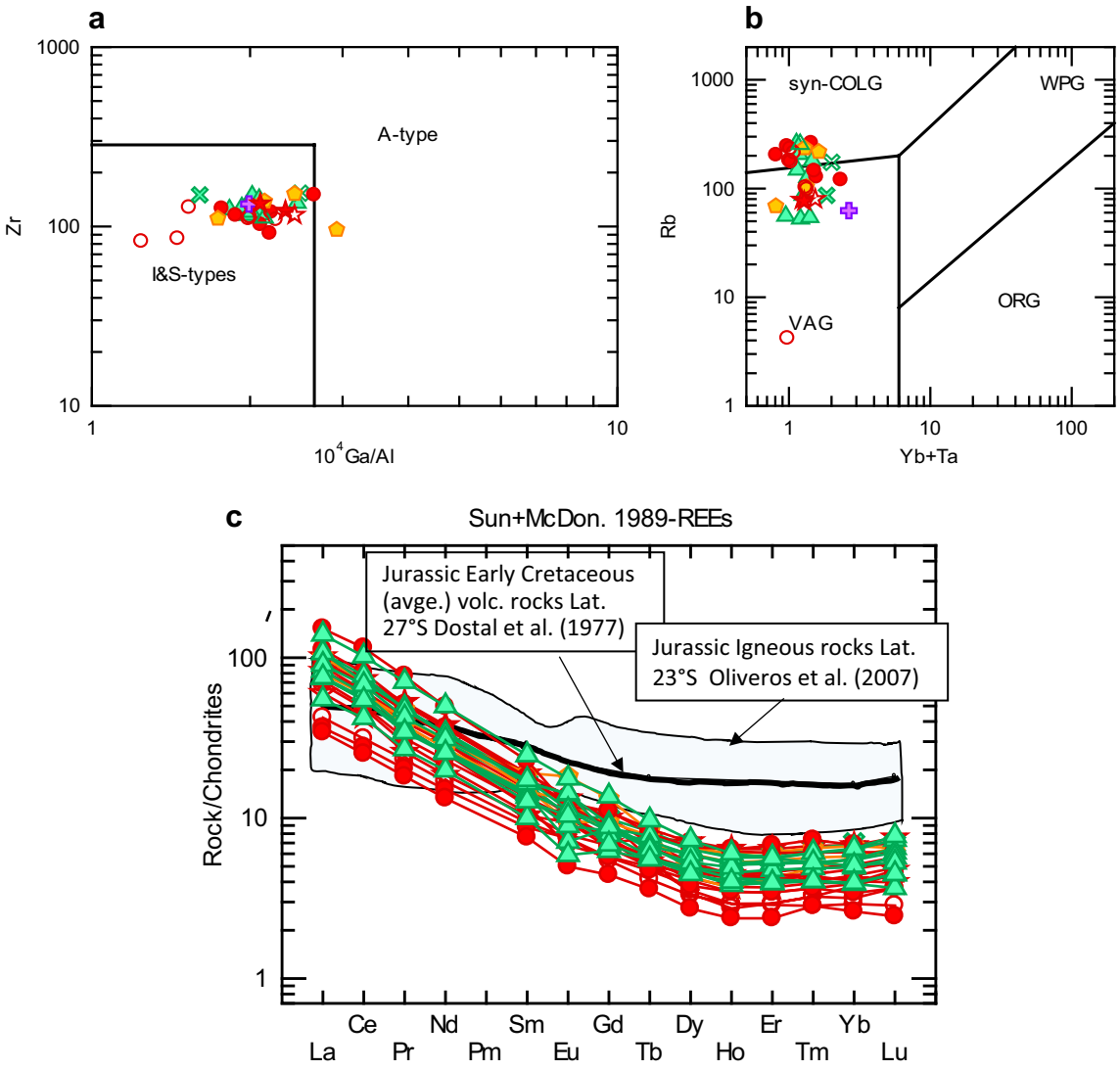

Fig. 8 Discriminant diagrams showing that MMH Triassic and Eocene–Oligocene rocks, as well as Chuquicamata *East and Banco Porphyries* are very similar in composition (recalculated volatile-free) and plot **a** in the field of I and S type granitoids and **b** straddle the fields of volcanic arc and syn-collision granitoids (Pearce et al. 1984); however, the Rb content may have been increased by alteration and volatile-free recalculation for rocks with high LOI (Table 2). **c** REE patterns (chondrite-normalized after Sun and McDonough 1989) of Triassic intrusions (green) and Eocene–Oligocene porphyries (red and yellow) overlap in composition. This pattern is generally interpreted as representing the effect of amphibole fractionation of oxidized magmas. Notice the clear distinction between MMH intrusives and Jurassic–Early Cretaceous volcanic rocks at Lat. 27°S (Dostal et al. 1977) and Jurassic intrusive and volcanic rocks along the coastal belt at the latitude 22–23°S (Oliveros et al. 2007). Legend as in Fig. 5

suggest that both magmas had a similar source and process of magma genesis.

The fact that the MMH, Chuquicamata host intrusives of Triassic and Eocene–Oligocene age are relatively low in Th and U and TiO_2 (Figs. 10, 11), irrespective of K_2O content, suggests this characteristic is a primary feature; the narrow range in Th/U ratio supports this hypothesis. This fact is remarkable because being more differentiated than many of the Fortuna–Los Picos Complex rocks (data in Ballard 2001), one would expect the rocks to have higher U and Th content (e.g., Larsen and Gottfried 1960). The uranium content of central Andean volcanic rocks is highest in regions with the thickest continental crust (Zentilli and Dostal 1977), hence the U and Th depletion suggests minimal crustal interaction. This concept is compatible with the available Pb, Sr, and Nd isotopic data for Chuquicamata (Zentilli et al. 1988; Maksaev 1990; Tosdal et al. 1999) and Os in the ores (Mathur et al. 2000; Zentilli et al. 2015), which suggest mantle-like affinities for the Chuquicamata porphyries. Although some rocks in the Fortuna Complex overlap in composition, within the actual Chuquicamata and MMH deposits this relative depletion in U and Th in host

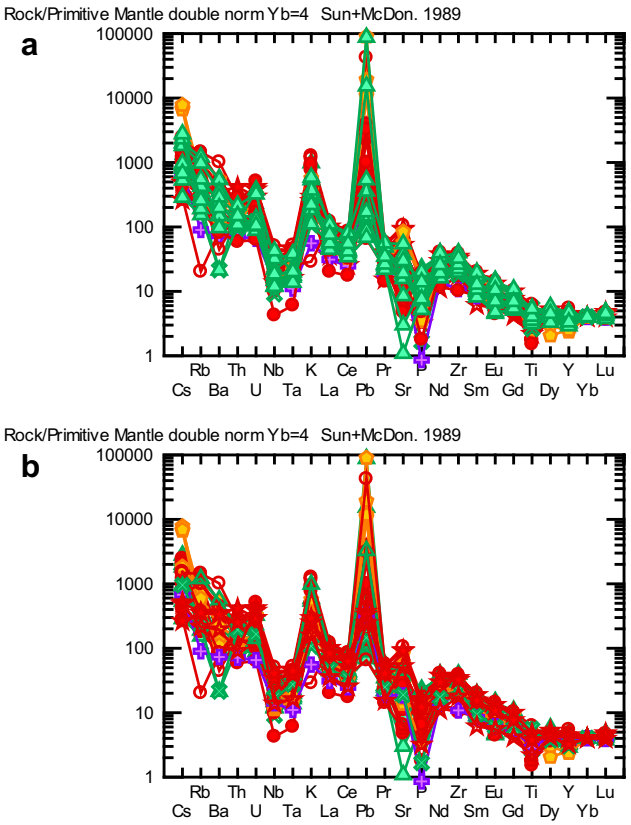

Fig. 9 Trace element plot (rock/primitive mantle double-normalized) after Sun and McDonough (1989). Note coincidence between most Triassic (green) and Eocene–Oligocene rocks (red–yellow). Note that **a, b** are the same samples, same plot, inverted back to front to emphasize the overlap. Legend as in Fig. 5

rocks may be empirically useful in mapping and exploration, for instance using a hand-held spectrometer that distinguishes gamma rays from U, Th and K.

The Triassic intrusives of MMH are so like Eocene–Oligocene porphyries, that it is probable that the conditions of magma generation were analogous. Porphyry Cu–Mo ore deposits are formed in the uppermost 4–5 km of the crust (with some, deeper, exceptions), and their ore zones are only a few km in the vertical dimension (e.g., Sillitoe 2010), hence their economic feasibility requires that post-ore erosion brings them close to the surface, but is not excessive as to remove the mineralized zone and expose the underlying (barren) batholith below (e.g., Wainwright et al. 2017). The Eocene–Oligocene PCDs in the Domeyko Cordillera were preserved because rates of exhumation decreased significantly after 31 Ma (e.g., Maksaev and Zentilli 1999). Even if Permo-triassic volcano-plutonic complexes of the Collahuasi Fm. around the Chuquicamata district (Fig. 2) did form PCDs, they were probably deeply eroded before the sea invaded the region to deposit the Caracoles Fm. in the Middle Jurassic (Bajocian, ca. 170 Ma; Tomlinson and Blanco 2008).

Was there a magmatic gap during the Rhaetian?

Although it is understood that subduction was almost continuous from the Paleozoic to the Mesozoic and the Holocene the model requires some refinement. The intrusion of the *MM Granodiorite* took place between 229 and ca. 207 Ma in the Late Triassic (Norian—perhaps Early Rhaetian considering the uncertainty of some dates). This time appears to coincide with the final magmatic episodes of the Gondwanan cycle, which had been active since the Carboniferous. Mpodozis and Kay (1992) suggested that between Triassic and Jurassic times there was a hiatus or very slow subduction. In this part of the Central Andes the prevalent tectonic regime was one of extension characterized by deposition of conglomerates that include erosional debris from the bimodal rhyolite-rich Choiyoi magmatism of the Paleozoic of Argentina and Chile and coal beds (e.g., Camus 2003; Maksaev et al. 2014; del Rey et al. 2016).

Magmatism was active in the Triassic, but towards the Rhaetian (now bracketed at 205.50 ± 0.35–201.36 ± 0.17 Ma; Wotzlaw et al. 2014) it became less intense. Vásquez et al. (2015) and Maksaev et al. (2007, 2014) have assembled an extensive database of ages that cover the Triassic and Jurassic; in their tables and diagrams, there seems to be a scarcity of ages of intrusives between ca. 207 and ca. 200 Ma. Espinoza et al. (2015) studied Triassic volcano-sedimentary basins in northern Chile between Latitudes 24.5°S and 26°S, and concluded they characterize continental sedimentary deposition during the Norian to Rhaetian, with the volcano-sedimentary units containing detrital zircons of Lower Ordovician and Permian age, denoting exhumation of the Paleozoic basement at that time. González et al. (2015) studied Triassic volcanic rocks in the Domeyko Cordillera between latitudes 24°30′ and 25°S, which they consider products of minor post-tectonic arc volcanism. About 500 km to the south, at latitude 27°S the La Ternera Fm. contains abundant plant remains and coal beds of Rhaetian age (e.g., Bell and Suárez 1995); it is composed of thick alluvial conglomerate and sandstones rich in quartz and rhyolite debris derived from erosion of the crystalline basement. However, at the type locality the coaly beds are overlain by basaltic andesites and in the higher Andes to the east the formation comprises thick volcanic units (Mpodozis et al. 2012; Iriarte et al. 1996) overlain by Lower Jurassic marine strata, hence the volcanic rocks are considered Triassic, although no dates are available. If future, reliable dating were to indicate Rhaetian magmatism, it may confirm the existence of latitudinal differences and tectonic segmentation as proposed by Franzese and Spalletti (2001).

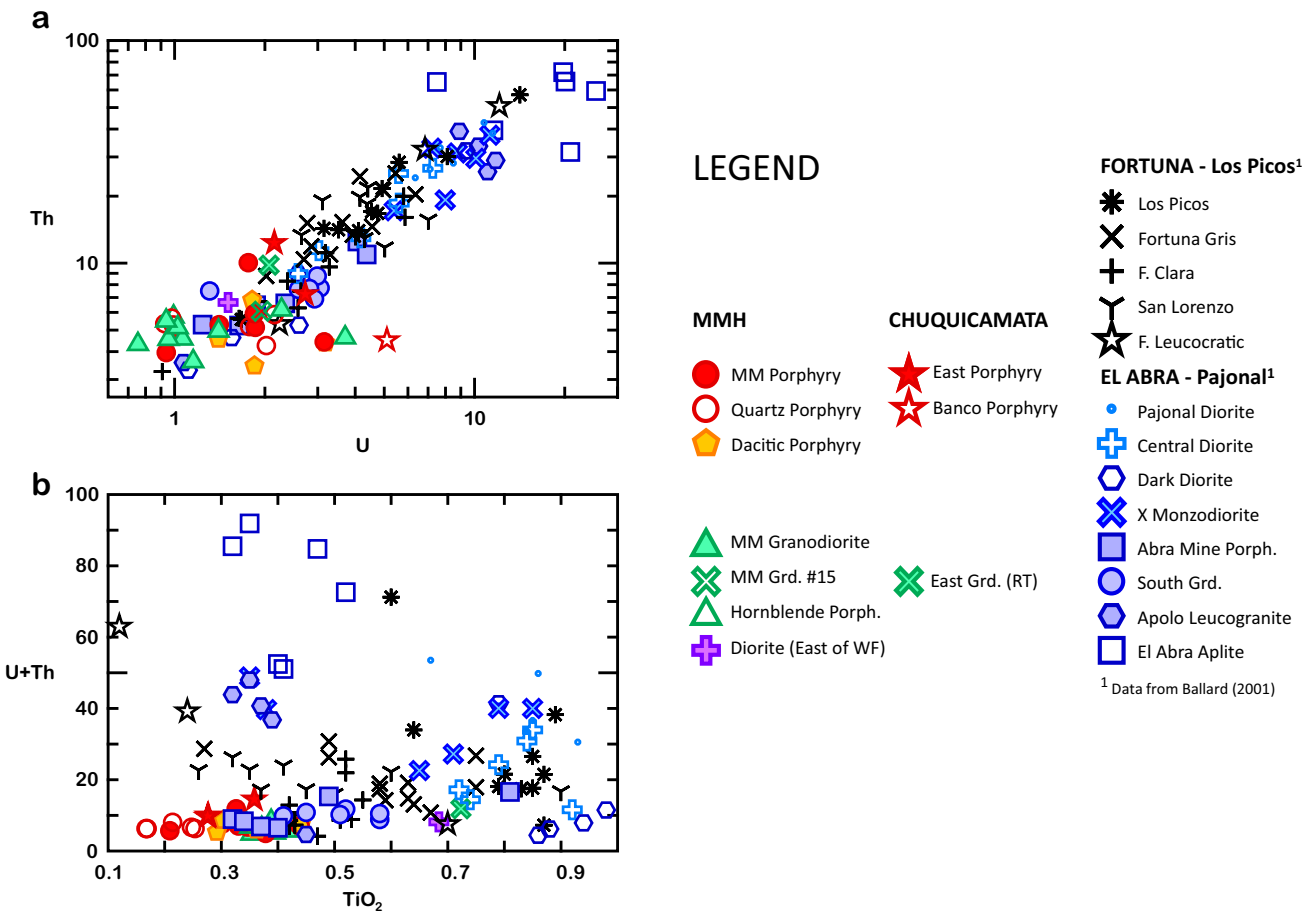

Fig. 10 Comparison of the MMH and Chuquicamata intrusives with other suites from the region, in terms of TiO_2, Th and U. The *Fortuna–Los Picos* intrusives lie west of the West Fault (Fig. 2) and El Abra Mine is located 45 km north of Chuquicamata (Fig. 1). **a** Notice the similarity of most Triassic and Eocene–Oligocene intrusions in the Chuquicamata District, and their relatively low content of Th and U. **b** Similar to the mineralized MMH and Chuquicamata porphyries (low TiO_2 and low Th + U) are the *El Abra Mine Porphyry* and the *Apolo Leucogranite* which contain the bulk of the ore at the El Abra PCD deposit (e.g., Campbell et al. 2006). Data and nomenclature for *Fortuna–Los Picos* and *El Abra–Pajonal* complexes from Table 5 in Ballard (2001)

Further south (latitude 28°–30°15′S) zircon ages by Hervé et al. (2014) show that the last magmatic pulse in the Triassic lasted from 225 to 215 Ma (Norian). During this time in central Chile and Argentina (30–40°S), there is evidence of very slow or arrested subduction, uplift and extension of the basement, basaltic underplating and crustal melting leading to bimodal volcanism (e.g., Gana 1991; Franzese and Spalletti 2001). Parada et al. (1997) proposed lithospheric delamination to explain the lack of arc magmatism during this time. In northern Chile subduction was active until the Late Norian, but in Peru, north of Cuzco, an earlier rift setting has been recognized, at least from 240 to 220 Ma (Lluis Fontboté. Pers. Comm.). The Rhaetian was characterized by extensional sedimentary basins with minor volcanic input, but again this volcanism had intraplate rift affinities and there is no evidence of a magmatic arc at the time (e.g., Rosas et al. 2007). The lull in subduction in northern Chile during the Rhaetian was probably related to global tectonic developments throughout Pangea at the time. Sealevel was near its lowest level in the Mesozoic between ca. 210 and 200 (Haq et al. 1988), possibly related to subdued seafloor spreading while ocean basins enlarged due to thermal subsidence (Embry 1988). Important petroleum reservoirs were formed in Rhaetian regressive sands in the Canadian Arctic Archipelago (Embry and Johannessen 1993). The Rhaetian (205.5–201.36 Ma; Wotzlaw et al. 2014) was the prelude of massive plate reorganization and the breakup of Pangea (e.g., Rona and Richardson 1978), which was marked by extensional faulting in Gondwana, the opening of the Atlantic Ocean and the catastrophic and simultaneous extrusion at ca. 201.5 Ma of giant flood basalt provinces (central Atlantic magmatic province: CAMP) from the north Atlantic (Nova Scotia), through Morocco to Bolivia (Tarabuco mafic sill, 500 km NE of Chuquicamata; Davies et al. 2017). This Rhaetian magmatism, is considered to have contributed to drastic climate change and the

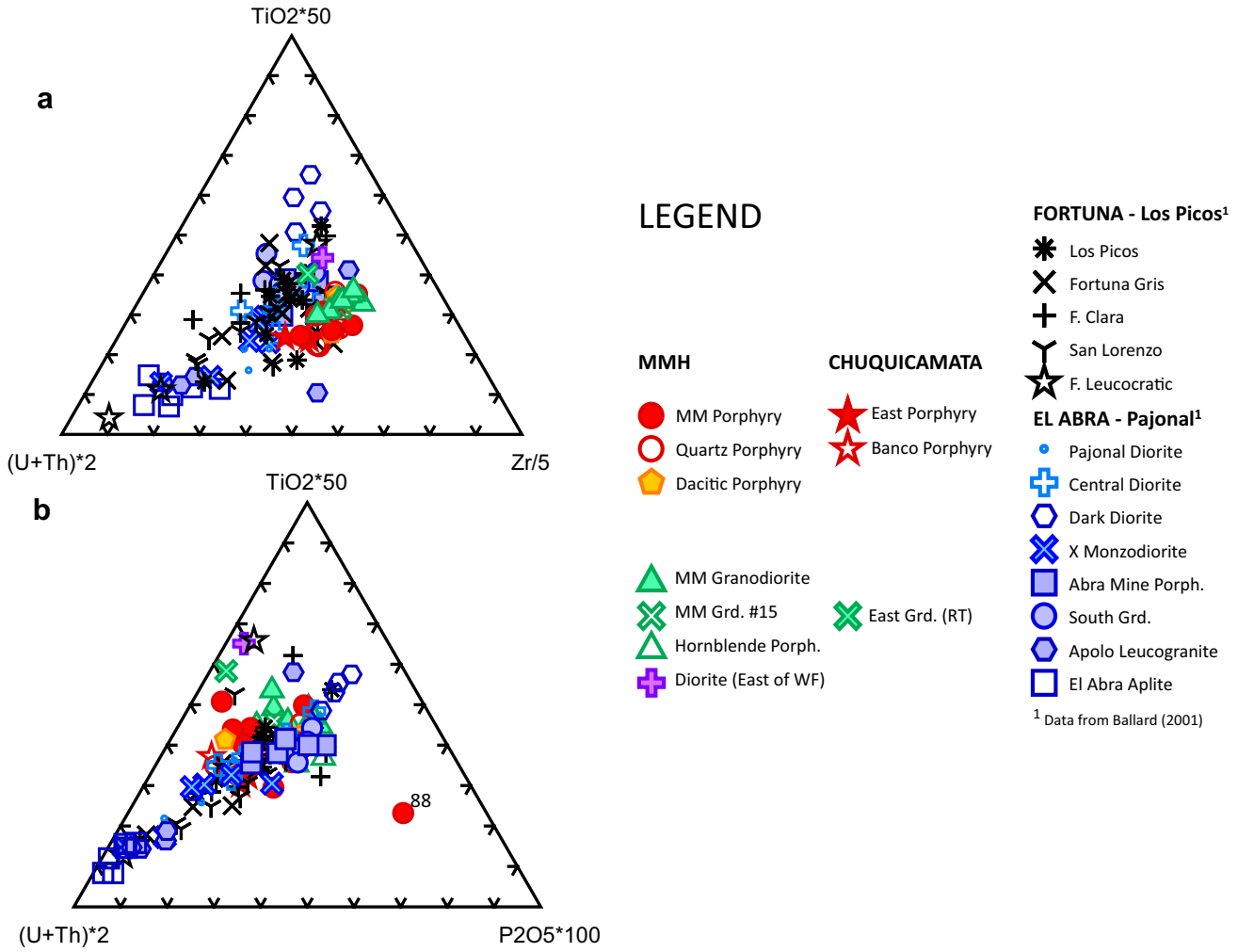

Fig. 11 Diagram comparing the MMH and Chuqui intrusives with the *Fortuna–Los Picos* and *El Abra–Pajonal* Complexes in terms of **a** U + Th, Zr (×2; in ppm) and TiO_2 (×50; in wt %) and **b** U + Th, TiO_2 and P_2O_5. All recalculated volatile-free. Note the similarity between Triassic and Eocene–Oligocene rocks at MMH and Chuquicamata. Altered MM Porphyry sample ZMMH-88 (labeled) is anomalously rich in P_2O_5 and Y (Fig. 5b, c). Also, note the similarity of rocks from MMH and Chuquicamata with those at El Abra Mine. Data and nomenclature for *Fortuna–Los Picos* and *El Abra–Pajonales* complexes from Table 5 in Ballard (2001). Legend as in Fig. 10

end-Triassic mass extinction during a low stand of sea level (Davies et al. 2017).

There has been ample discussion of the tectonic conditions active in the central Andes during the Eocene–Oligocene and the influence of oblique subduction and the ascent of magmas controlled by the orogen-parallel Domeyko Fault system a dextral, ductile to brittle shear system (e.g., Lindsay et al. 1995; Maksaev and Zentilli 1999; Tomlinson and Blanco 2008); it is possible that Triassic magmas also took advantage of such deep regional fracture systems to ascend and form a relatively narrow igneous belt (Fig. 1). For the area to the south, between latitudes 30° and 40°S, Franzese and Spalletti (2001) propose the existence of dextral shear system along the western margin of Gondwana during the Late Triassic to Early Jurassic; it is possible that this shear system extended farther north. A sinistral orogen-parallel shear system (Atacama Fault System) related to oblique subduction was active in the Jurassic–Cretaceous (Hervé 1987; Jaillard et al. 1990; Pichowiak 1994) and was responsible for the localization of important iron–oxide–copper–gold deposits and manto type Cu deposits (e.g., Maksaev and Zentilli 2002; Sillitoe 2003; Cembrano et al. 2005).

Between ca. 210 and ca. 200 Ma the main magmatic front moved westward about 100 km so that by the beginning of the "Andean" subduction cycle in the Early Jurassic it was located near the present coast (Fig. 1). There was considerable uncertainty in older geochronological methods; Maksaev (1990) reported dates as old as 200 Ma for intrusive and volcanic rocks along the coast, although Vásquez et al. (2015) obtained younger dates in the same area (Toarcian; ca. 183 Ma). Lower Jurassic igneous rocks along the coast are drastically different from Upper

Triassic intrusives (e.g., Dostal et al. 1977; Rossel et al. 2015) in the Chuquicamata District (Fig. 8c); the Jurassic rocks have been grouped as La Negra Fm. representing large outpours of basaltic to andesitic lavas with flat REE patterns akin to those of island arcs. Models proposed for the igneous rocks vary from mantle-like arc magmatism related to a thin crust (e.g., Charrier et al. 2007; Oliveros et al. 2007); a back-arc regime (Rogers and Hawkesworth 1989; Kramer et al. 2005), or a product of pull-apart basins related to oblique subduction (Jaillard et al. 1990; Pichowiak 1994). This shift of the magmatic front suggests a rollback (Fig. 12) from an Andean-type subduction to a much steeper Mariana-type subduction (e.g., Uyeda 1982), the configuration suggested for central Chile in the Jurassic–Cretaceous (Åberg et al. 1984). Slab rollback, as happened in the Mariana arc, can occur in as little as a few million years (Straub et al. 2015). Sedimentation patterns

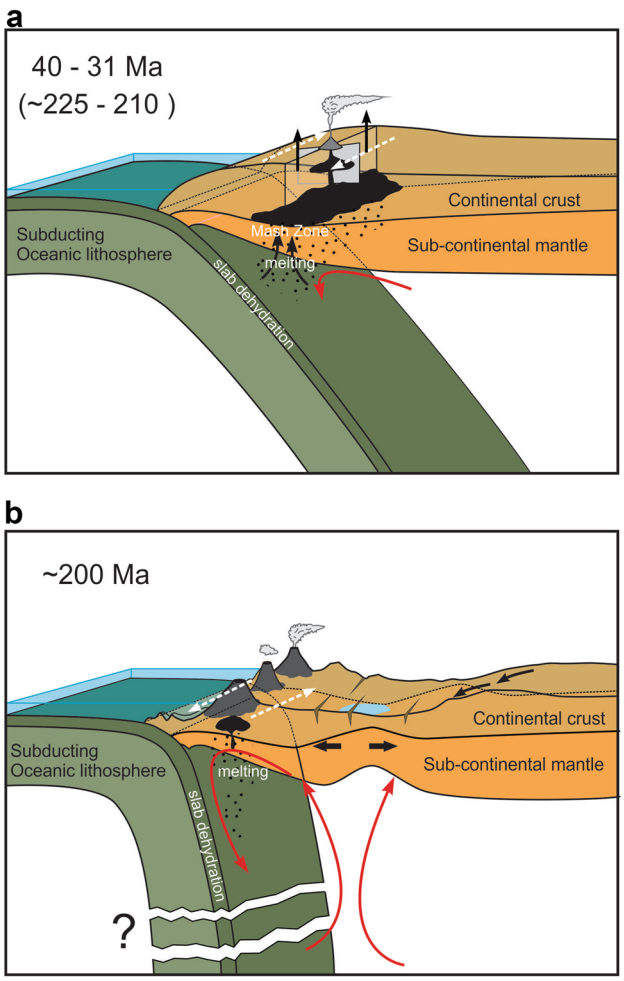

Fig. 12 Cartoon contrasting the probable subduction configuration at the South American margin of northern Chile **a** during the Norian and Eocene–Oligocene and **b** during the earliest Jurassic, with the volcanic front along the coastal range, after rollback. Modified from Richards (2003), Franzese and Spalletti (2001) and Uyeda (1982)

suggest that in the Jurassic the back-arc region became a marginal basin, representing extension and no mountain building (Scheuber and Gonzalez 1999; Tomlinson and Blanco 2008; Martínez et al. 2017).

Both the Upper Triassic and Eocene–Oligocene intrusives in the Domeyko Cordillera, which were favorable to mineralization show some interesting similarities in terms of tectonics. Both were emplaced at the termination or waning stage of a magmatic cycle, just preceding a break in major igneous activity that was followed by a major shift of the magmatic front, ca. 100 km westward before the Jurassic, and ca. 20 km (and beyond) eastward before the Miocene, and a drastic change in magma chemistry (e.g., Boric et al. 1990; Maksaev 1990). The dextral orogen-parallel Domeyko Fault System, of which the West Fault is a brittle expression, was a deep fracture that controlled the ascent and emplacement of magmas into N–S elongated plutons and determined the permeability for hydrothermal alteration and mineralization in the Chuquicamata District (Lindsay et al. 1995; Maksaev and Zentilli 1999). It is reasonable to propose that the Late Triassic (Carnian–Norian) magmatic arc exploited a similar deeply reaching fracture system.

The last igneous activity in the Chuquicamata district is represented by the *Oeste and Banco Porphyries* in Chuquicamata and *Quartz Porphyry* and *Dacite Porphyry* at MMH (35.3–33.7 Ma, respectively), and the last hydrothermal mineralization was formed at ca. 31 Ma (Ossandón et al. 2001; Reynolds et al. 1998; Ballard et al. 2001), all under a dextral regime of the Domeyko Fault System (Lindsay et al. 1995); This interval represents a time of rapid exhumation that coincides with the Incaic orogenic phase in the Central Andes (Maksaev 1990; Maksaev and Zentilli 1999; McInnes et al. 1999; Martínez et al. 2017). The cessation of major hydrothermal activity at 31 Ma in the Domeyko Cordillera was followed by left-lateral movement across the fault system, which attained a net 35 Km displacement (Tomlinson and Blanco 1997, 2008). After an apparent hiatus in igneous activity, with infrequent volcanic activity (e.g., San Pedro Fm. tuffs; K–Ar 28.6–24.9 Ma; Marinovic and Lahsen 1984) the magmatic front jumped in the Early Miocene some 20 km eastward to near the Holocene volcanic front (Fig. 1) and extended hundreds of kilometers into Bolivia and Argentina, with the extrusion of andesites and massive silicic ignimbrites of predominantly Late Miocene to early Pliocene age (ca. 10–5 Ma; e.g., Maksaev 1990; Coira et al. 1982; Wotzlaw et al. 2011). This Early Miocene magmatic flare-up event coincides in time with accelerating, more orthogonal, Farallon/Nazca–South America plate convergence, suggesting a positive feedback between convergence rates and a major tectonic readjustment and an increase in crustal thickness (Mamani et al. 2010) and production of magmas in the Central Andes and as far north as Ecuador (e.g., Schütte et al. 2010).

Conclusions

1. Whole rock geochemistry on a representative set of zircon U–Pb dated intrusive rocks of the Chuquicamata District reveals that the long-lasting difficulty experienced by geologists in differentiating Triassic from Eocene intrusive host intrusive rocks in MMH and other giant Cu–Mo deposits in the District is due to the fact that these rocks are almost indistinguishable in major, minor and trace-element composition. Accordingly, they react similarly to hydrothermal alteration.
2. However, the most voluminous *MM Porphyry* can be distinguished from Triassic *MM Granodiorite* by comparing their relatively higher content of Fe_2O_3 and Ni (Fig. 6), and Al_2O_3 and TiO_2: in general, the *MM Granodiorite* contains more than 15 wt% Al_2O_3, and less than 0.33 wt% TiO_2 (Fig. 7a–d). Iron and Ni could be easily analyzed during routine operations. In terms of petrography, the Eocene *MM Porphyry* contains identifiable megacrysts of sphene (titanite) whereas the Triassic *MM Granodiorite* does not.
3. Oligocene *Dacitic Porphyry* dikes in MMH overlap somewhat in composition with the Triassic *MM granodiorite*, but have physical characteristics that make them easily recognizable. Chemically, *Dacitic Porphyry* is anomalous in its elevated content of cesium (Cs), more than 20 ppm, double that of other rocks. It is also relatively rich in Fe_2O_3, S and Sb, in part carried in sulfides. However, it is poor in Cu, Mo and other useful metals, hence we interpret the *Dacitic Porphyry* dikes to have been emplaced later than the main phases of mineralization.
4. If magma character determines the ability of a system to generate giant Cu–Mo deposits, then Carnian–Norian rocks may have also hosted important Cu–Mo deposits; their preservation will depend on their post-ore erosional history and subsequent cover.
5. The voluminous *MM Porphyry* at MMH is practically indistinguishable from the equally important *Este Porphyry* of Chuquicamata and RT mines. Both yield dates of ca. 36–35 Ma. supporting the hypothesis that they are one and the same intrusion, separated by the West Fault after the end of the mineralization process, as proposed by Zentilli et al. (2015).
6. The U and Th content of host Triassic and Eocene–Oligocene mineralized rocks in MMH, Chuquicamata and RT is relatively low compared to most of the intrusive rocks from the district. In the El Abra district, 45 km north of Chuquicamata, low U and Th is shown mainly in mineralized hosts. This empirical low content in radioactive U and Th in prospective rocks could be investigated as a potential geochemical and geophysical exploration tool.
7. At the latitude of the Chuquicamata, Late Triassic subduction-related magmatism (Carnian to Norian; the age of *MM Granodiorite* at MMH and *Este and Elena Granodiorites* of Chuquicamata) District was analogous to that of the Eocene–Oligocene, and both were intruded within the same narrow belt in the mineral fertile Domeyko Cordillera. The Eocene–Oligocene magma emplacement and mineralization were controlled by a deep ductile to brittle orogen-parallel fracture system (the Domeyko Fault System), created by oblique subduction; it is probable that the Late Triassic magmatism took advantage of the same crustal structures, possibly also enhanced by oblique subduction.
8. Between the intrusion of the youngest of the Norian intrusives in MMH (ca. 207 Ma) and the onset of Jurassic subduction magmatism (ca. 200 Ma) there was a westward shift of the magmatic front of about 100 km, probably a plate rollback. Subduction changed from Andean-type to steep, Mariana-type subduction. This shift followed a pause in energetic magmatism, coincident with extensive basement erosion and accumulation of sediments in extensional basins of Rhaetian age. The Rhaetian stage (205.5–201.36 Ma; Wotzlaw et al. 2014) coincides with a worldwide ocean low stand, probably a lull in seafloor spreading and Andean subduction, and precedes the catastrophic outpour of massive basaltic magmas from the north Atlantic to Bolivia at ca. 201.5 Ma, roughly coinciding with drastic climate change and the Triassic–Jurassic mass extinction (e.g., Davies et al. 2017).
9. Similarly, the Eocene–Oligocene magmatism responsible for the formation of the MMH, Chuquicamata and RT deposits in the Chuquicamata District was the last gasp of activity ending at ca. 31 Ma, followed by a lull in magmatism and a 20-km shift, this time eastwards, of the magmatic front, coinciding with a change in the magmatic character of the rocks and in intensity of plate interaction; post-Oligocene plate reorganization caused a 2- to 3-fold increase in convergence rate between the Nazca Plate and South American plates (e.g., Muñoz et al. 2000). It appears that the formation of giant Cu–Mo PCDs was enhanced during the waning stages of a long-standing magmatic system.

Acknowledgements We thank MMH and Corporación del Cobre (CODELCO) staff, especially Jaime Diaz-Acevedo, whose extensive knowledge of the mine geology made this study possible. Pedro Elisetche for representative samples of Radomiro Tomic mine. We thank Jaroslav (Jarda) Dostal for motivating us to study trace element geochemistry of volcanic rocks. Milton C. Graves for brainstorming, project management and hard work during initial research on the

Chuquicamata District. Ian Campbell for permitting the use of unpublished data from a PhD thesis (ANU) by Julian R. Ballard. We thank Lluis Fontboté for his thorough and constructive reviews, and Ryan Mathur, Jamie Wilkinson and Matt Loader for helpful suggestions that enhanced the manuscript. Map figures were drafted by Randall Cormier SMU, Halifax. The research was funded by CODELCO's Gerencia de Recursos Mineros y Desarrollo Distrital as a research contract with MZGeoscience Inc. of Halifax, Canada.

References

Åberg G, Aguirre L, Levi B, Nystrom JO (1984) Spreading subsidence and generation of ensialic marginal basins, an example from the Early Cretaceous of central Chile. Geol Soc Spec Publ 16:185–193

Ambrus J (1979) Emplazamiento y mineralización de los pórfidos cupríferos de Chile. Unpublished Ph.D. thesis, Universidad de Salamanca, Salamanca, Spain, p 308 **(in Spanish)**

Arnott AM (2003) Evolution of the hydrothermal alteration at the Chuquicamata porphyry copper system, northern Chile. Unpublished PhD Thesis, Dalhousie University, Halifax, Nova Scotia, Canada, p 455

Arnott AM, Zentilli M (2003) The Chuquicamata intrusive complex: its relation to the Fortuna Intrusive Complex, and the role of the Banco Porphyry in the potassic alteration zone. Actas, X Congreso Geológico Chileno, Concepción, p 10

Ballard JR (2001) A comparative study between the geochemistry of the ore-bearing and barren calc-alkaline intrusions. Unpublished PhD Thesis, Australian National University, Canberra, p 255

Ballard JR, Palin JM, Williams IS, Campbell IH, Faunes A (2001) Two ages of porphyry intrusion resolved for the super-giant Chuquicamata copper deposit of northern Chile by ELA-ICP-MS and SHRIMP. Geology 29:383–386

Barra F, Alcota H, Rivera S, Valencia V, Munizaga F, Maksaev V (2013) Timing and formation of porphyry Cu–Mo mineralization in the Chuquicamata district, northern Chile: new constraints from the Toki cluster. Miner Deposita 48:629–651

Bell CM, Suárez M (1995) Triassic alluvial braidplain and braided river deposits of the La Ternera Formation, Atacama region, northern Chile. J S Am Earth Sci 8:1–8

Boric R, Díaz F, Maksaev V (1990) Geología y Yacimientos Metalíferos de la Región de Antofagasta. SERNAGEOMIN, Santiago, Chile, Boletín 40, p 246 **(in Spanish)**

Boric R, Diaz J, Becerra H, Zentilli M (2009) Geology of the Ministro Hales Mine (MMH), Chuquicamata district, Chile, S11-055. XII Congreso Geológico Chileno, Santiago, pp 1–4

Buchelt M, Tellez-Cancino C (2006) The Jurassic La Negra Formation in the area of Antofagasta, northern Chile (lithology, petrography, geochemistry) (1988). In: Bahlburg H, Breitkreuz C, Giese P (eds) The Southern Central Andes-lecture notes in Earth sciences 17. Springer, Heidelberg, pp 171–182

Campbell IH, Ballard JR, Palin JM, Allen C, Faunes A (2006) U–Pb zircon geochronology of granitic rocks from the Chuquicamata-El Abra porphyry copper belt of Northern Chile: Excimer laser ablation ICP-MS analysis. Econ Geol 101:1327–1344

Camus F (2003) Geología de los Sstemas Porfíricos en los Andes de Chile. SERNAGEOMIN, Santiago, p 267 **(in Spanish with English Abstract)**

Cembrano J, González J, Arancibia G, Ahumada I, Olivares I, Herrera V (2005) Fault zone development and strain partitioning in an extensional strike-slip duplex: a case study from the Mesozoic Atacama Fault System, Northern Chile. Tectonophysics 400:105–125

Charrier R, Pinto L, Rodríguez MP (2007) Tectonostratigraphic evolution of the Andean Orogen in Chile. In: Moreno T, Gibbons W (eds) The geology of Chile. The Geological Society, London, pp 21–114

Clark AH, Farrar E, Caelles JC, Haynes SJ, Lortie R, McBride SL, Quirt S, Robertson RCR, Zentilli M (1976) Longitudinal variations in the metallogenetic evolution of the Central Andes: a progress report. Geol Assoc Can Spec Pap 14:25–58

Cohen KM, Harper DAT, Gibbard PL (2017) ICS International Chronostratigraphic Chart 2017/02. International Commission on Stratigraphy, IUGS. http://www.stratigraphy.org. Accessed 20 Feb 2018

Coira B, Davidson J, Mpodozis C, Ramos V (1982) Tectonic and magmatic evolution of the Andes of northern Argentina and Chile. Earth Sci Rev 18:303–332

Coloma F, Valin X, Oliveros V, Vásquez P, Creixell C, Salazar E, Ducea M (2017) Geochemistry of Permian to Triassic igneous rocks from northern Chile (28°–30°15′S): implications on the dynamics of the proto-Andean margin. Andean Geol 44:147–178

Contreras JF, González R, Wilke HG (2015) Registros triásicos de depósitos volcánicos-piroclásticos dentro de una configuración lacustre, Cordillera de Domeyko, Antofagasta. Norte de Chile. Actas, XIV Congreso Geológico Chileno, La Serena, Chile, pp 871–873 **(in Spanish)**

Cornejo P, Matthews S, Marinovic N, Pérez de Arce C, Basso M, Alfaro J, Navarro M (2006) Alteración hidrotermal y mineralización recurrente de Cu y Cu–Mo durante el pérmico y el triásico en la Cordillera de Domeyko (zona de Zaldívar-Salar de los Morros): antecedentes geocronológicos U–Pb, $^{40}Ar/^{39}Ar$ y Re–Os, 2. Actas, XI Congreso Geológico Chileno, Antofagasta, pp 219–222 **(Spanish with English abstract)**

Davies JHFL., Marzoli A, Bertrand H, Youbi N, Ernesto M, Schaltegger U (2017) End-Triassic mass extinction started by intrusive CAMP activity. Nat Commun 8:15596. https://doi.org/10.1038/ncomms15596

del Rey A, Deckart K, Arriagada C, Martínez F (2016) Resolving the paradigm of the late Paleozoic–Triassic Chilean magmatism: isotopic approach. Gondwana Res 37:172–181

Dilles JH, Tomlinson AJ, Martin MW, Blanco N (1997) El Abra and Fortuna Complexes: A porphyry copper batholith sinistrally displaced by the Falla Oeste. Actas, VIII Congreso Geológico Chileno, Antofagasta, vol 3, pp 1883–1887

Dostal J, Zentilli M, Caelles JC, Clark AH (1977) Geochemistry of volcanic rocks of the Andes between 26° and 28° South. Contr Mineral Petrol 63:113–128

Embry AF (1988) Triassic sea-level changes: evidence from the Canadian Arctic Archipelago. In: Sea-level changes—an integrated approach. The Society of Economic Paleontologists and Mineralogists. SEPM Special Publication No 42, Tulsa, pp 249–259

Embry AF, Johannessen EP (1993) T–R sequence stratigraphy, facies analysis and reservoir distribution in the uppermost Triassic–Lower Jurassic succession, Western Sverdrup Basin, Arctic Canada. Norwegian Petroleum Society Special Publications, Elsevier, Amsterdam, vol 2, pp 121–146

Espinoza M, Oliveros V, Vásquez P, Bechis F (2015) U–Pb geochronology and kinematic preliminary analyses of Late Triassic–Early Jurassic basins in northern Chile (24.5°–26°S). Actas, XIV Congreso Geológico Chileno, La Serena, Chile, pp 840–843

Farrar E, Clark AH, Haynes SJ, Quirt S, Conn H, Zentilli M (1970) K–Ar evidence for the post Paleozoic migration of granitic intrusion foci in the Andes of northern Chile. Earth Planet Sci Lett 10:60–66

Faunes A, Hintze F, Siña A, Veliz H, Vivanco M (2005) Chuquicamata, core of a planetary scale Cu–Mo anomaly. In: Porter TM (ed) Super porphyry copper and gold deposits—a global perspective, vol 1. PGC, Adelaide, pp 151–174

Franzese JR, Spalletti LA (2001) Late Triassic–Early Jurassic continental extension in southwestern Gondwana: tectonic segmentation and pre-break-up rifting. J S Am Earth Sci 14:257–270

Gana P (1991) Magmatismo bimodal del Triásico superior–Jurásico inferior en la Cordillera de la Costa, Provincia de Elqui y Limarí. Revista Geológica de Chile 18:55–68 **(Spanish with English abstract)**

González O, Menzies A, González R, le Roux P, Janney P, Wilke HG (2015) Nuevos antecedentes geoquímicos acerca de la transición entre el magmatismo Paleozoico Superior–Triásico en la Cordillera de Domeyko (24°30′–25°S). XIV Congreso Geológico Chileno, La Serena, Chile, pp 844–847 **(in Spanish with English abstract)**

González-Maurel O, Menzies AH, González R, le Roux PJ (2016) Understanding the onset of Andean subduction: new Sr and Nd isotopic data from late Paleozoic to late Triassic magmatism in northern Chile. International Geological Congress, paper (No. 2525)

Haq BU, Hardenbol J, Vail PR (1988) Mesozoic and Cenozoic chronostratigraphy and cycles of sea-level change. Sea-level changes—an integrated approach, SEPM Special Publication No. 42, pp 71–108

Heaman LM, Erdmer P, Owen JV (2002) U–Pb geochronologic constraints on the crustal evolution of the Long Range Inlier, Newfoundland. Can J Earth Sci 39:845–865

Hervé M (1987) Movimiento sinistral en el Cretácico Inferior de la Zona de Falla Atacama al Norte de Paposo (24°S), Chile. Revista Geológica de Chile 31:37–42 **(Spanish with English abstract)**

Hervé F, Fanning CM, Calderón M, Mpodozis C (2014) Early Permian to Late Triassic batholiths of the Chilean Frontal Cordillera (28°–31°S): SHRIMP U–Pb zircon ages and Lu–Hf and O isotope systematics. Lithos 184–187: 436–446

Horstman EL (1957) The distribution of lithium, rubidium and caesium in igneous and sedimentary rocks. Geochim Cosmochim Acta 12:1–28

Iriarte S, Arévalo C, Mpodozis C, Rivera O (1996) Mapa Geológico de la Hoja Carrera Pinto. Servicio Nacional de Geología y Minería, Santiago, p 3

Ishihara S, Ulriksen CE, Sato K, Terashima S, Sato T, Endo Y (1984) Plutonic rocks of north-central Chile. Bull Geol Surv Jpn 35:503–536

Jaillard E, Soler P, Carlief G, Mourner T (1990) Geodynamic evolution of the northern and central Andes during early to middle Mesozoic times: a Tethyan model. Geol Soc Lond 147:1009–1022

Jaillard E, Hérail G, Monfret T, Díaz-Martínez E, Baby P, Lavenu A, Dumont JF (2000) Tectonic evolution of the Andes of Ecuador, Peru, Bolivia and northernmost Chile. In: Cordani UG, Milani EJ, Thomaz Filho A, Campos DA (eds) "Tectonic evolution of South America". Sociedade Brasileira de Geologia XXXI International Geological Congress, Rio de Janeiro, Brazil, pp 481–559

James DE (1971) Plate tectonic model for evolution of Central Andes. Geol Soc Am Bull 82:3325–3346

Jordan TE, Isacks BL, Allmendinger RW, Brewer JA, Ramos VA, Ando CJ (1983) Andean tectonics related to geometry of subducted Nazca plate. Geol Soc Am Bull 94:341–361

Kramer W, Ehrlichmann R (1996) Geochemical evolution of Triassic and Jurassic volcanic successions in Northern Chile between 20° and 26°30′ latitude south. Third ISAG, Sr Malo, France, 17–19/9/1996, pp 593–596

Kramer W, Siebel W, Romer RL, Hasse G, Zimmer M, Ehrlichman R (2005) Geochemical and isotopic characteristics and evolution of the Jurassic volcanic arc between Arica (18°30′S) and Tocopilla (22°S), North Chilean Coastal Cordillera. Chemie der Erde-Geochemistry 65:47–78

Larsen ES, Gottfried D (1960) Uranium and thorium in selected suites of igneous rocks. Bradley Volume. Am J Sci 258A:151–169

Lee RG, Dilles JH, Tosdal RM, Wooden JL, Mazdab FK (2017) Magmatic evolution of granodiorite intrusions at the El Salvador Porphyry copper deposit, Chile, based on trace element composition and U/Pb age of Zircons. Econ Geol 112:245–273

Levi B (1973) Eastward shift of mesozoic and early tertiary volcanic centers in the coast range of central Chile. Geol Soc Am Bull 84:3901–3910

Lindsay DD (1997) Structural control and anisotropy of mineralization within the Chuquicamata porphyry copper deposit, northern Chile. Unpublished PhD Thesis, Dalhousie University, Halifax, Nova Scotia, Canada, 404p

Lindsay DD, Zentilli M, Rojas J (1995) Evolution of an active ductile to brittle shear system controlling mineralization at the Chuquicamata porphyry copper deposit, northern Chile. Int Geol Rev 37:945–958

Lucassen F, Kramer W, Bartsch V, Wilke HG, Franz G, Romer RL, Dulski P (2006) Geochemical evolution of Triassic and Jurassic volcanic successions in Northern Chile between 20° and 26°30′ latitude south. Contrib Mineral Petrol 152:571–589

Maksaev V (1990) Metallogeny, geological evolution and thermochronology of the Andes between latitudes 21° and 26° south, and the origin of major porphyry copper deposits. Unpublished PhD Thesis, Dalhousie University, Halifax, Nova Scotia, Canada, p 544

Maksaev V, Zentilli M (1988) Metallogenic framework of the large porphyry copper deposits of the Andes of northern Chile. In: Proceedings, V Congreso Geológico Chileno, Santiago, Chile, I: B181–B212 **(in Spanish, with English abstract)**

Maksaev V, Zentilli M (1999) Fission track thermochronology of the Domeyko Cordillera, northern Chile: Implications for Andean tectonics and porphyry copper metallogenesis. Explor Min Geol 8:65–89

Maksaev V, Boric R, Zentilli M, Reynolds PH (1988) Metallogenic implications or K–Ar, Ar^{40}–Ar^{39} and fission track dates of mineralized areas in the Andes of northern Chile. Actas, V Congreso Geológico Chileno, Santiago, pp B65–B86

Maksaev V, Zentilli M (2002) Chilean Strata-bound Cu-(Ag) Deposits: An Overview. In: Porter TM (ed) Hydrothermal iron oxide copper-gold & related deposits: a global perspective, vol 2. PGC Publishing, Adelaide, Australia, pp 185–205

Maksaev V, Townley B, Palacios C, Camus F (2007) Metallic ore deposits. In: Moreno T, Gibbons W (eds) The geology of Chile. The Geological Society, London, pp 179–199

Maksaev V, Munizaga F, Tassinari C (2014) Timing of the magmatism of the paleo-Pacific border of Gondwana: U–Pb geochronology of Late Paleozoic to Early Mesozoic igneous rocks of the north Chilean Andes between 20° and 31°S. Andean Geol 41:447–506

Mamani M, Wörner G, Sempere T (2010) Geochemical variations in igneous rocks of the Central Andean orocline (13°S to 18°S): tracing crustal thickening and magma generation through time and space. GSA Bull 122:162–182

Marinovic S, Lahsen A (1984) Hoja Calama. Carta Geol de Chile 58. SERNAGEOMIN, Santiago, p 140

Martínez F, Parra M, Arriagada C, Mora A, Bascuñán S, Peña M (2017) Late Cretaceous to Cenozoic deformation and exhumation of the Chilean Frontal Cordillera (28º–29ºS), Central Andes. J Geodyn. https://doi.org/10.1016/j.jog.2017.08.004

Mathur R, Ruiz J, Munizaga F (2000) Relationship between copper tonnage of Chilean base-metal porphyry deposits and Os isotope ratios. Geology 28:555–558

May G, Hartley A, Chong G, Stuart F, Turner P, Kape S (2010) Eocene to Pleistocene lithostratigraphy, chronostratigraphy and tectonosedimentary evolution of the Calama Basin, northern Chile. Revista Geológica de Chile 32:33–58

McInnes BIA, Farley KA, Sillitoe RH, Kohn BP (1999) Application of apatite (U–Th)/He thermochronometry to the determination of the sense and amount of vertical fault displacement at

the Chuquicamata porphyry copper deposit, Chile. Econ Geol 94:937–948

Mortimer BC, Münschmeyer FC, Urqueta DI (1978) Emplazamiento del yacimiento Exótica, Chile. Revista Geológica de Chile 6:41–51 **(in Spanish with English abstract)**

Mpodozis C, Cornejo P (2012) Cenozoic tectonics and porphyry copper systems of the Chilean andes. In: Hedenquist JW, Harris M, Camus F (eds) Geology and genesis of major copper deposits and districts of the World: a tribute to Richard H Sillitoe. Society of Economic Geologists, Littleton, Special Publication 16, pp 329–360

Mpodozis C, Kay SM (1992) Late Paleozoic to Triassic evolution of the Gondwana margin: Evidence from Chilean Frontal Cordilleran batholiths (28°S to 31°S). Geol Soc Am Bull 104:999–1014

Mpodozis C, Ramos VA (1990) The Andes of Chile and Argentina. In: Ericksen GE, Pinochet MT, Reinemund JA (eds) Geology of the Andes and its relation to hydrocarbon and mineral resources. Circum-Pacific Council for Energy and Mineral Resources, Earth Science Series, Houston, pp 59–90

Mpodozis C, Iriarte S, Gardeweg M, Valenzuela M (2012) Carta Laguna del Negro Francisco. Servicio Nacional de Geología y Minería. Carta Geológica de Chile, Serie Geología Básica 145

Munizaga F, Maksaev V, Fanning CM, Giglio S, Yaxley G, Tassinari CCG (2008) Late Paleozoic–Early Triassic magmatism on the western margin of Gondwana: Collahuasi area, Northern Chile. Gondwana Res 13:407–427

Muñoz J, Troncoso R, Duhart P, Crignola P, Farmer L, Stern CR (2000) The relation of the mid-Tertiary coastal magmatic belt in south-central Chile to the late Oligocene increase in plate convergence rate. Revista Geológica de Chile 27(2):177–203

Oliveros V, Morata D, Aguirre L, Féraud G, Fornari M (2007) Jurassic to Early Cretaceous subduction-related magmatism in the Coastal Cordillera of northern Chile (18°30′–24°S): geochemistry and petrogenesis. Revista Geológica de Chile 34:209–232

Ossandón G, Zentilli M (1997), El distrito de Chuquicamata: una concentración de cobre de clase mundial: Congreso Geológico Chileno, VIII, Antofagasta, v. III, pp 1888–1892 **(in Spanish)**

Ossandón G, Fréraut R, Gustafson L, Lindsay D, Zentilli M (2001) Geology of the Chuquicamata mine: a progress report. Econ Geol 96:240–270

Parada MA, Nystrom JO, Levi B (1997) The role of lithospheric delamination during the evolution of the coastal batholith of central Chile (31 to 34°S). Actas, 3. VIII Congreso Geológico Chileno, Antofagasta, pp 1699–1703

Parada MA, Lopez-Escobar L, Oliveros V, Fuentes F, Morata D, Calderon M, Aguirre L, Féraud G, Espinoza F, Moreno H, Figueroa O, Muñoz-Bravo J, Troncoso-Vásquez R, Stern CR (2007) Andean magmatism. In: Moreno T, Gibbons W (eds) The geology of Chile. The Geological Society, London, pp 115–146

Pearce JA (1996) A user's guide to basalt discrimination diagrams. In: Wyman DA (ed) Trace element geochemistry of volcanic rocks: applications for massive sulphide exploration, vol 12. Geological Association of Canada, Short Course Notes, pp 79–113

Pearce JA, Harris NBW, Tindle AG (1984) Trace element discrimination diagrams for the tectonic interpretation of granitic rocks. J Petrol 25:956–983

Peccerillo A, Taylor SR (1976) Geochemistry of Eocene calc-alkaline volcanic rocks from the Kastamonu area, Northern Turkey. Contrib Mineral Petrol 58:63–81

Pichowiak S (1994) Early Jurassic to early Cretaceous magmatism in the coastal cordillera and the central depression of north Chile. In: Tectonics of the southern Central Andes. Springer, Berlin Heidelberg, pp 203–217

Pinget M-C (2016) Supergene enrichment and exotic mineralization at Chuquicamata, Chile. Unpublished PhD Thesis, Faculté des Sciences, Université de Genève, Switzerland, 145 p

Pinget M-C, Dold B, Zentilli M, Fontboté L (2015) Reported supergene sphalerite rims at the Chuquicamata porphyry deposit (northern Chile) revisited: evidence for a hypogene origin. Econ Geol 110(1):253–262

Proffett JM (2008) Geologic review of the MM deposit, Chuquicamata District, Chile. Unpublished internal report for CODELCO, p 13

Proffett JM, Dilles JH (2007) Shrimp-RG ion microprobe U–Pb age determinations of intrusive rock units northeast of the Chuquicamata Mine, Chile. Unpublished internal report for CODELCO, p 15

Reutter K, Scheuber E, Chong G (1996) The Precordilleran fault system of Chuquicamata, northern Chile: evidence for reversals along arc-parallel strike-slip faults. Tectonophysics 259:213–228

Reynolds P, Ravenhurst C, Zentilli M, Lindsay DD (1998) High precision $^{40}Ar/^{39}Ar$ dating of two consecutive hydrothermal events in the Chuquicamata porphyry copper system. Chile Chem Geol 148:45–60

Richards JP (2003) Tectono-magmatic precursors for porphyry Cu–(Mo–Au) deposit formation. Econ Geol 98:1515–1533

Rivera S, Alcota H, Proffett J, Díaz J, Leiva G, Vergara M (2012) Update of the Geologic Setting and Cu–Mo Deposits of the Chuquicamata District, Northern Chile. In: Harris M, Camus F (eds) Geology and Genesis of major copper deposits and districts of the world: a tribute to Richard H. Sillitoe and J.W. Hedenquist. Society of Economic Geologists, Special Publication No.16, pp 19–54

Rogers G, Hawkesworth CJ (1989) A geochemical traverse across the North Chilean Andes: evidence for crust generation from the mantle wedge. Earth Planet Sci Lett 91:271–285

Rona PA, Richardson ES (1978) Early Cenozoic global plate reorganization. Earth Planet Sci Lett 40:1–11

Rosas S, Fontboté L, Tankard A (2007) Tectonic evolution and paleogeography of the Mesozoic Pucará Basin, central Peru. J S Am Earth Sci 24:1–24

Rossel P, Oliveros V, Ducea MN, Hernandez L (2015) Across and along arc geochemical variations in altered volcanic rocks: Evidence from mineral chemistry of Jurassic lavas in northern Chile, and tectonic implications. Lithos 239:97–113

Ruiz C, Ericksen GE (1962) Metallogenetic provinces of Chile, South America. Econ Geol 57:91–106

Scheuber E, Gonzalez G (1999) Tectonics of the Jurassic–Early Cretaceous magmatic arc of the north Chilean Coastal Cordillera (22°–26°S): a story of crustal deformation along a convergent plate boundary. Tectonics 18:895–910

Scheuber E, Bogdanic T, Jensen A, Reutter KJ (1994) Tectonic Development of the North Chilean Andes in relation to plate convergence and magmatism since the Jurassic. In: Reutter JJ, Scheuber E, Wigger PJ (eds) Tectonics of the Southern Central Andes. Springer, Berlin, pp 121–139

Schütte P, Chiaradia M, Beate B (2010) Geodynamic controls on Tertiary arc magmatism in Ecuador: Constraints from U–Pb zircon geochronology of Oligocene–Miocene intrusions and regional age distribution trends. Tectonophysics 489:159–176

Sillitoe RH (1972) Relation of metal provinces in western America to subduction of oceanic lithosphere. Geol Soc Am Bull 83:813–818

Sillitoe RH (1977) Permo-Carboniferous, late Cretaceous and Miocene porphyry copper-type mineralization in the Argentinian Andes. Econ Geol 72:99–103

Sillitoe RH (1988) Epochs of intrusion-related copper mineralization in the Andes. J South Am Earth Sci 1:89–108

Sillitoe RH (2003) Iron–oxide–copper–gold deposits: an Andean view. Miner Deposita 38:787–812

Sillitoe RH (2010) Porphyry copper systems. Econ Geol 105:3–41

Sillitoe RH, Perelló J (2005) Andean copper province: Tectonomagmatic settings, deposit types, metallogeny, exploration, and

discovery. In: Hedenquist JW, Thompson JFH, Goldfarb RJ, Richards JP (eds) Economic geology 100th anniversary volume. Society of Economic Geologists, Littleton, Colorado, pp 845–890

Sillitoe RH, Marquardt JC, Ramírez F, Becerra H, Gómez M (1996) Geology of the concealed MM porphyry copper deposit, Chuquicamata District, northern Chile. In: Camus F, Sillitoe RH, Petersen R (eds) Andean copper deposits: new discoveries, mineralization styles and metallogeny. Society of Economic Geologists, Special Publication 5, pp 59–70

Simonetti A, Heaman LM, Hartlaub RP, Creaser RA, McHattie T, Böhm C (2005) Rapid and precise U–Pb zircon dating by laser ablation MC-ICP-MS using a new multiple ion counting-faraday collector array. J Anal Atom Spectrosc 20:677–686

Spikings A, Reitsma MJ, Boekhout F, Mišković A, Ulianov A, Chiaradia M, Gerdes A, Schaltegger U (2016) Characterisation of Triassic rifting in Peru and implications for the early disassembly of western Pangaea. Gondwana Res 35:124–143

Straub SM, Woodhead JD, Arculus RJ (2015) Temporal evolution of the Mariana Arc: mantle wedge and subducted slab controls revealed with a tephra perspective. J Petrol 56:409–439

Sun S, McDonough WF (1989) Chemical and isotopic systematics of oceanic basalts: implications for mantle composition and processes. In: Saunders AD, Norry MJ (eds) Magmatism in the Ocean Basins, vol 42. Geological Society, London, Special Publications, pp 313–345

Tobey EF (2005) Interim report on mineralogy and geochemistry at Mansa Mina. Unpublished report by GEOVECTRA for CODELCO, p 115

Tomlinson AJ, Blanco N (1997) Structural evolution and displacement history of the West Fault System, Pre-cordillera. Chile. Actas. VIII Congreso Geológico Chileno 3:1873–1878, 1878–1882

Tomlinson AJ, Blanco N (2008) Geología de la franja Chuquicamata-El Abra, (21°45′ 22°30′ S), II Región. SERNAGEOMIN, Santiago, Chile. Informe Registrado IR-08-35, p 196 **(in Spanish)**

Tomlinson AJ, Blanco N, Maksaev V, Dilles JH, Grunder A, Ladino M (2001) Geología de la Precordillera Andina de Quebrada Blanca-Chuquicamata, Regiones I y II (20°30′–22°30′S). Servicio Nacional de Geología y Minería (SERNAGEOMIN), Santiago, Chile, Informe Registrado IR-01-20, 20 mapas escala 1:50.000, p 444

Tosdal RM, Wooden JL, Bouse RM (1999) Pb isotopes, ore deposits, and Metallogenic Terranes, application of radiogenic isotopes to ore deposit research and exploration. Rev Econ Geol 12:1–28

Uyeda S (1982) Subduction zones: an introduction to comparative subductology. Tectonophys 81:133–159

Vásquez P, Sepúlveda FA, Quezada A (2015) 110 millones de años de volcanismo andesítico (Triásico Superior–Cretácico Inferior) en la Cordillera de la Costa (20°00′–21°15′S): nuevas edades U/Pb. In: XIV Congreso Geologico Chileno, La Serena, Chile, pp 848–851

Wainwright AJ, Tosdal RM, Lewis PD, Friedman RM (2017) Exhumation and preservation of the porphyry Cu–Au deposits at Oyu Tolgoi, South Gobi region, Mongolia. Econ Geol 112:591–601

Wilson J, Zentilli M, Boric R, Diaz J, Maksaev V (2011) Geochemistry of the Triassic and Eocene igneous host rocks of the MMH porphyry copper deposit, Chuquicamata District, Chile. In: Proceedings, 11th SGA Biennial meeting, let's talk ore deposits, Antofagasta, Chile, pp 426–428

Winchester JA, Floyd PA (1977) Geochemical discrimination of different magma series and their differentiation products using immobile elements. Chem Geol 20:325–343

Wotzlaw JF, Decou A, von Eynatten H, Wörner G, Frei D (2011) Jurassic to Palaeogene tectono-magmatic evolution of northern Chile and adjacent Bolivia from detrital zircon U–Pb geochronology and heavy mineral provenance. Terra Nova 23:399–406

Wotzlaw JF, Guex J, Bartolini A, Gall Y, Krystyn L, McRoberts CA, Taylor D, Schoene B, Schaltegger U (2014) Towards accurate numerical calibration of the Late Triassic: High-precision U–Pb geochronology constraints on the duration of the Rhaetian. Geology 42:571–574

Zentilli M (2012) Nuevos antecedentes geoquímicos y metalogénicos-yacimiento MMH. Gerencia de Recursos Mineros y Desarrollo Distrital, CODELCO, p 151 **(unpublished report)**

Zentilli M, Dostal J (1977) Uranium in volcanic rocks from the central Andes. J Volcanol Geoth Res 2(3):251–258

Zentilli M, Doe BR, Hedge C, Alvarez O, Tidy E, Daroca JA (1988) Isótopos de plomo en yacimientos de tipo pórfido cuprífero comparados con otros depósitos metalíferos de los Andes de Chile y Argentina. Actas V Congreso Geológico Chileno Santiago Chile 1B:331–369 **(in Spanish with English abstract)**

Zentilli M, Krogh TE, Maksaev V, Alpers CN (1994) Uranium-lead dating of zircons from the Chuquicamata and La Escondida porphyry copper deposits, Chile: inherited zircon cores of Paleozoic age with Tertiary overgrowths, vol 45. Comunicaciones, Universidad de Chile, Santiago, pp 101–110

Zentilli M, Boric R, Heaman L, Mathur R, Hanley J (2015) New developments on the geology of MMH: is it the "missing half" of Chuquicamata? In: Extended abstract, actas, XIV Chilean geological congress, symposium 2, Exploración Andina: Nuevos Hallazgos y Actualizaciones. La Serena, Chile, p 4

Affiliations

Marcos Zentilli[1] · Victor Maksaev[2] · Ricardo Boric[3] · Jessica Wilson[1,4]

Victor Maksaev
vmaksaev@ing.uchile.cl

Ricardo Boric
Ricardo.boric@angloamerican.com

Jessica Wilson
jwilson8891@gmail.com

[1] Department of Earth Sciences, Dalhousie University, Halifax, NS B3H 4R2, Canada

[2] Departamento de Geología, Universidad de Chile, Plaza Ercilla 803, Santiago, Chile

[3] Angloamerican, Santiago, Chile

[4] Indigenous and Northern Affairs Canada, Yellowknife, NT X1A 0B4, Canada